JJEE
Volume 11 | Number 4 | Pages 776-805

Jordan Journal of Electrical Engineering

ISSN (print): 2409-9600, ISSN (online): 2409-9619

Homepage: jjee.ttu.edu.jo

Watermarking and Reconstructing Multi-channel Images in the Transform Domain with Application to Diabetic Retinopathy Medical Images

Yasser Fouda[1*]

[1] Mathematics Department, Faculty of Science, Mansoura University, Mansoura, Egypt
E-mail: ymafouda@mans.edu.eg

Received: May 17, 2025 *Revised: Oct 27, 2025* *Accepted: Nov 14, 2025* *Available online: Jan 20, 2026*

***Abstract*—** This paper introduces a transformative watermarking technique tailored for multi-channel images, utilizing discrete Krawtchouk moments to capture intricate features in medical images. The method facilitates seamless watermark embedding in the transform domain, preserving the diagnostic integrity of medical images. The proposed scheme offers a robust framework for watermark insertion and extraction, resilient against twelve types of attacks. Beyond watermarking, our approach extends to reconstructing multi-channel images, a significant advancement in medical imaging. This enables clinicians to recover pristine images for precise diagnostics while ensuring data security. Experimental evaluations on an 89-image diabetic retinopathy dataset confirm the efficacy of our techniques, showcasing the ability to embed and extract watermarks without compromising diagnostic quality and successfully reconstruct original images.

***Keywords*—** Medical images; Image watermarking; Color image reconstruction; Transform domain.

1. INTRODUCTION

In recent years, the rapid advancement of medical imaging technologies has revolutionized the field of healthcare by providing physicians with invaluable tools for diagnosis, treatment planning, and monitoring of various medical conditions. With the increasing adoption of digital imaging modalities, such as Magnetic Resonance Imaging (MRI), Computed Tomography (CT), Ultrasound and Diabetic Retinopathy Medical Images (DRMI), the demand for secure and reliable methods to store, transmit, and protect medical images has become paramount. One significant concern in the digital era is the protection of medical images against unauthorized access, tampering, and forgery. To address this issue, digital watermarking has emerged as a promising solution. Watermarking techniques enable the embedding of imperceptible yet robust information, known as watermarks, into the host images. These watermarks can serve as digital signatures to authenticate the images' integrity, ownership, and origin.

A digital image watermark is a technology used to protect the ownership of digital images (Jing et al. [1]). It finds widespread application in copyright protection and image traceability. Traditional watermarking techniques (Fares et al. [2]; Su et al. [3]; Rakhmawati et al. [4]; Hu et al. [5]; Wang et al. [6]; Liu et al. [7]) achieve copyright protection by adding watermark information to medical images. However, this approach necessitates modifications to the content of medical images, which can compromise the integrity of the images. These

* Corresponding author
DOI: https://doi.org/10.5455/jjee.204-1747483516

modifications can disrupt the data structure of original medical images and impact the diagnosis of healthcare professionals. To address the challenge of balancing robustness and invisibility in traditional watermarking technology, several authors, including Daoui et al. [8] and Lang and Zhang [9], have proposed transformation domain watermarking schemes. These schemes utilize the feature information of images to develop watermarking techniques that achieve copyright protection without the need for image content modification. This approach offers a significant advantage in preserving the integrity of medical data, making it a widely adopted method for copyright protection in the field of medical images (Xia et al. [10], Liu et al. [11], and Wu et al. [12]).

In the realm of medical imaging, the challenge lies not only in watermarking single-channel images but also in preserving the rich diagnostic information contained in multi-channel medical images. Multi-channel medical images, such as multi-slice CT scans or multi-contrast DRMI images, provide complementary and essential information for accurate diagnosis and treatment planning. Therefore, any watermarking technique applied to such images must ensure that the embedded watermarks do not compromise the diagnostic quality and integrity of the underlying data.

This article proposes a novel watermarking scheme for multi-channel medical images in the transform domain using discrete orthogonal Krawtchouk polynomials. The Krawtchouk transform, a generalized orthogonal transform, offers excellent energy compaction and decorrelation properties, making it suitable for efficient representation of medical image data. By utilizing the Krawtchouk moments, the proposed scheme aims to embed watermarks imperceptibly across the multiple channels of DRMI medical images, while ensuring robustness against various attacks and maintaining the diagnostic quality of the reconstructed images. The main objectives of this research can be summarized in three parts: (1) to develop an effective image watermarking scheme that can securely embed and extract watermarks in multi-channel medical images using the Krawtchouk transform, and (2) to evaluate the performance of the proposed scheme in terms of imperceptibility and robustness, and (3) to give a high-precision reconstruction for DRMI images using discrete orthogonal moments.

The rest of this article is organized as follows: In Section 2, we present an overview of related work in medical image watermarking and its reconstruction, highlighting the limitations of existing techniques. Section 3 provides a detailed explanation of the proposed color image reconstruction algorithm in the transform domain, as well as the proposed image watermarking scheme, encompassing both watermark embedding and extraction processes. Section 4 presents the experimental results and discusses the evaluation metrics employed to assess the performance of the proposed scheme. Finally, in Section 5, we summarize the key findings and contributions of the article.

2. RELATED WORK

The field of medical image watermarking has received significant attention in recent years due to increasing concerns over the security and integrity of medical data. Various techniques have been proposed to address the challenges associated with watermarking multi-channel medical images, with a focus on preserving diagnostic quality while ensuring robustness against attacks. In this section, we provide an overview of the existing literature related to watermarking and reconstruction of multi-channel medical images, particularly in the transform domain. The utilization of image moments in medical image reconstruction is

widespread. When these moments are not orthogonal, reconstructing an image from them becomes a challenging task. Moments based on continuous orthogonal polynomials necessitate precise approximations of integrals and appropriate transformations of image coordinates in space. This significantly increases computational costs and introduces errors in discretization, potentially leading to inaccuracies in computed moments [9, 10, 13]. To address this challenge, a set of discrete orthogonal moments, including Charlier [41], Tchebichef [42], Meixner [14], Krawtchouk [15], and Hahn [16], has been proposed for digital image reconstruction. The use of discrete orthogonal polynomials as kernel functions for computing image moments eliminates the need for numerical approximations and ensures exact orthogonality within the discrete domain of image space coordinates. This property renders discrete orthogonal moments superior to continuous orthogonal moments in terms of image reconstruction capabilities. However, it's important to note that the use of these discrete orthogonal moments incurs a high computational cost due to the involvement of hypergeometric functions. To mitigate this error and improve the accuracy of image reconstruction, we employ the three-term recurrence relation and benefit by the diagonal symmetry of Krawtchouk polynomials.

In their publication [17], Singh et al. authored a textbook focusing on watermarking techniques and their applications in medical images. Their work offers a comprehensive exploration of medical image watermarking approaches within both the spatial and transformation domains. The authors provide a succinct overview of various watermarking attacks and discuss the key metrics employed to evaluate the performance of watermarking algorithms. Notably, they delve into multiple watermarking techniques that utilize eye images as covers, facilitating secure and efficient transmission of medical data, particularly in tele-ophthalmology applications. Mousavi et al. [18] conducted a survey on watermarking methods applied to medical images, wherein they analyzed the strengths and weaknesses of each approach. They outlined the fundamental components of a typical watermarking system and elucidated the system's basic requirements. Additionally, they delved into the key metrics for assessing the visual quality of watermarked images and the accuracy of retrieved watermarks. It's worth noting that while this survey offered valuable insights, it did not include empirical results or numerical analyses of watermarking algorithms. In their study [19], Nyeem et al. conducted a review of security measures and their prerequisites for safeguarding medical images in the context of teleradiology. They also assessed the potential threats anticipated in teleradiology setups and identified the limitations of conventional security measures in addressing these threats. Furthermore, they conducted a comprehensive examination of digital watermarking techniques tailored for teleradiology. Lastly, the authors delineated the fundamental objectives of medical image watermarking in teleradiology and provided a summary of recommended watermarking methods and their characteristics. In their work [20], Abraham et al. introduced a color image watermarking scheme implemented in the spatial domain. Their focus was on harnessing spatial domain techniques to enhance the robustness of image protection. Similar to methods employed in the transformation domain, their approach involves gradually dispersing watermark information across a pixel region. This approach aims to ensure the verification of two critical attributes: high image quality and resilience against various attacks. Additionally, the authors proposed the utilization of two masks, one for color compensation and another for watermark embedding. In their study [21], Fridrich et al. introduced two methodologies for lossless embedding, applicable not only to

digital images but also to digital video and audio. They adhered to fundamental principles as guiding criteria, resulting in the development of straightforward, efficient, and high-capacity lossless embedding techniques. These techniques were designed to accommodate the three most prevalent image format paradigms: raw, palette formats (such as GIF and PNG), transform formats (like JPEG), and uncompressed formats (such as BMP). The paper concludes by illustrating how the concept of lossless data embedding serves as a potent tool, enabling the accomplishment of various non-trivial tasks, including elegant lossless authentication using fragile watermarks. Eltoukhy et al. [22] introduced an image watermarking technique designed to enhance the security of color medical images. This approach combines the Slant transform, Quaternion Fourier-Transform (QFT), and Singular Value Decomposition (SVD). The process involves dividing the host image into four quarters, with one-time padding employed for encryption. The Slant transform is then applied to the encrypted sections, followed by the application of SVD to these transformed segments. Subsequently, the Quaternion Fourier Transform is applied. SVD is utilized to compress the binary watermark, which is further scrambled using the Arnold transform before being embedded into the modified Quaternion Fourier-Transform coefficients. To extract the watermark, the reverse operations of the embedding procedure are performed.

To enhance the security of medical images and safeguard copyright, Wu et al. [23] introduced a zero-watermarking algorithm based on the Dual-Tree Complex Wavelet Transform (DT CWT). This algorithm extracts low-frequency information from medical images using the DT CWT and employs an improved differential entropy method to select stable sub-blocks. To ensure the robust security of the zero-watermarking algorithm, it incorporates both a logistic chaotic map and Arnold scrambling mechanisms for watermarking. Experimental results demonstrated a high level of robustness, with a normalized cross-correlation (NCC) coefficient of 0.9928. Eswaraiah and Reddy [24] introduced a medical image watermarking algorithm that utilizes the integer wavelet transform (IWT). This algorithm not only verifies the integrity of the region of interest (ROI) but also identifies any tampered blocks within the ROI, enhancing the security of data embedded within the region of non-interest (RONI). The process involves segmenting the medical image into distinct ROI and RONI regions. Subsequently, the algorithm embeds the hash value of the ROI, recovery data of the ROI, and the patient's data into the RONI using the IWT technique. This approach ensures the preservation of critical information within the ROI and provides robust protection against tampering, thereby maintaining the integrity of the medical image data.

In image watermarking schemes based on moment transforms, various researchers have explored Harmonic transformation moments, including Polar Harmonic Transforms [31], Polar Complex Exponential Transforms [30], Ternary Radial Harmonic Fourier Moments [29], Bessel-Fourier Moments [28], Quaternion Exponent Moments [27], Legendre Moments [26], and Zernike Moments [25]. These moments serve to extract image features, thereby enhancing the watermarking scheme's robustness against geometric attacks. However, traditional techniques exhibit high computational complexity in computing their kernel functions and are prone to numerical instability, which can reduce the accuracy of image reconstruction. To address these challenges, Xia et al. [32] introduced Decimal-order Polar Harmonic Transforms Moments to enhance resistance against geometric attacks. Meanwhile, Yang et al. [33] proposed a Fast Quaternion Polar Complex Exponential Transformation to overcome the

computational costs associated with traditional moment transformations. In their work [31], they introduced the decimal polarization state into the polar harmonic transformation and constructed three distinct transformation forms. These three types of transformations are employed for feature extraction and to construct multiple zero-watermarking, demonstrating robustness under common image processing conditions, albeit with some limitations against small intensity attacks. In a different approach, Yamni et al. [34] presented an image watermarking technique based on Fractional Charlier Moments. This method involves computing eigenvectors and eigenvalues for each image block and utilizing a score factor to calculate the score eigenvalues of the image. The scheme generates an eigenvalue matrix based on the relationship between fractional eigenvalues and the mean of image moments. Moment-based image watermarking schemes, including those by Xia et al. [32], Yang et al. [33], and Yamni et al. [34], exhibit strong robustness against geometric attacks due to their independence and geometric invariance.

Several watermarking methods have been explored for single-channel medical images. For instance, frequency domain techniques, such as discrete Fourier transform (DFT) and discrete wavelet transform (DWT), have been widely utilized. Kahlessenane et al. [35] proposed a DWT-based method that embeds watermarks into the wavelet coefficients of medical images. Their scheme achieved robustness against common attacks but suffered from perceptual distortion. Dong et al. [36] presented a DFT-based method that utilized phase scrambling and LFSR techniques to embed watermarks. While their approach exhibited good robustness, it incurred a higher computational cost. In the context of multi-channel medical images, the challenges are more complex. Zermi et al. [37] proposed a watermarking scheme for multi-slice CT images using the singular value decomposition (SVD) technique. By embedding watermarks in the singular vectors of each slice, their method achieved a balance between robustness and perceptual quality. However, their scheme was limited to CT images and did not consider other modalities. To address the limitations of existing techniques, this article introduces a novel watermarking scheme that utilizes the Krawtchouk transform for embedding watermarks in multi-channel medical images. The Krawtchouk transform, a generalized orthogonal transform, offers excellent energy compaction and decorrelation properties, making it well-suited for efficient representation of medical image data. By leveraging the Krawtchouk coefficients, the proposed scheme aims to embed imperceptible watermarks across multiple channels while maintaining the diagnostic quality and robustness against attacks.

3. THE PROPOSED TECHNIQUES

In this section, we delve into two subsections to present our contributions. In the first subsection, we begin by introducing the discrete Krawtchouk polynomials and their moments on 2-D images. Subsequently, we propose an algorithm for reconstructing color images using Krawtchouk moments. Moving to the second subsection, we unveil a novel color image watermarking scheme that harnesses the potential of Krawtchouk moments and their inverses.

3.1. Color Image Reconstruction in the Moment-Transformed Domain

Discrete moment-based approaches have gained significant popularity in grayscale and color image processing due to their ability to compactly represent digital images. These

approaches characterize grayscale and color images by treating their shapes as mathematical functions and computing integrals of these image functions multiplied by specific kernel functions. Among these transformed image functions, discrete Krawtchouk moments hold particular importance. Krawtchouk polynomials $K_m(x;q,M)$are a set of discrete orthogonal polynomials characterized by their order m and a parameter q. They are known for satisfying the general first-order partial difference equation:

$$\sigma(\mathrm{x})\Delta\nabla y(x) + \varphi(x)\Delta y(x) + \eta_m y(x) = 0 \quad (1)$$

with

$$\sigma(x) = (1-q)x, \quad (2)$$

$$\varphi(x) = (-x + Mq), \quad (3)$$

$$\eta_m = m. \quad (4)$$

Then $K_m(x;q,M)$ can be written in Eq. (1) as:

$$(1-q)x\Delta\nabla K_m(x;q,M) + (-x+Mq)\Delta K_m(x;q,M) + mK_m(x;q,M) = 0 \quad (5)$$

With

$$x, m = 1,2,\dots,M;\ 0 < q < 1. \quad (6)$$

And

$$\Delta g(x) = g(x+1) - g(x), \quad (7)$$

$$\nabla g(x) = g(x) - g(x-1), \quad (8)$$

$$\Delta\nabla g(x) = g(x+1) - 2g(x) + g(x-1). \quad (9)$$

The one-dimensional discrete Krawtchouk polynomials of degree m can be represented by a hyper-geometric function as:

$$K_m(x;q,M) = {}_2F_1\left(-m,-x;-M;\frac{1}{q}\right) = \sum_{k=0}^{m}\frac{(-m)_k(-x)_k}{(-M)_k(k!)}\left(\frac{1}{q}\right)^k \quad (10)$$

where

$(-x)_k$ is a Pochhammer function and defined by:

$$(-x)_k = \prod_{i=1}^{k}(-x+i-1) \quad (11)$$

It is evident that the range of Krawtchouk polynomials in Eq. (10) expands rapidly with increasing degree m. Moreover, these polynomials face numerical instability for large values of M. As a result, a more stable set of polynomials can be derived from the conventional Krawtchouk polynomials by normalizing them with their norms and scaling them by the square root of a weight function. The weighted Krawtchouk polynomials $\widetilde{K}_m(x;q,M)$ are then defined as follows:

$$\widetilde{K}_m(x;q,M) = \sqrt{\frac{w(x;q,M)}{\rho(m;q,M)}}K_m(x;q,M), \quad (12)$$

where

$$w(x;q,M) = \binom{M}{x}(1-q)^{M-x}q^x, \quad (13)$$

$$\rho(m;q,M) = (-1)^m\frac{m!}{(-M)_m}\left(\frac{1-q}{q}\right)^m. \quad (14)$$

The new set of discrete weighted Krawtchouk polynomials in Eq. (12) satisfies the orthogonal condition:

$$\sum_{x=1}^{M}\widetilde{K}_m(x;q,M)\widetilde{K}_{m'}(x;q,M) = \delta_{mm'}. \quad (15)$$

To compute the discrete weighted Krawtchouk polynomials in Eq. (12), a three-term recurrence relation derived from Eq. (1) can be employed. The recursive computation based on this recurrence relation is more efficient than directly computing high-degree polynomials using Eq. (10). Such a recurrence relation is given by:

$$m\widetilde{K}_m(x;q,M) = \alpha_m\widetilde{K}_{m-1}(x;q,M) - \beta_m\widetilde{K}_{m-2}(x;q,M), \quad (16)$$

with initial conditions

$$\widetilde{K}_0(x;q,M) = \sqrt{\frac{w(x;q,M)}{\rho(0;q,M)}}, \tag{17}$$

$$\widetilde{K}_1(x;q,M) = (x(1-q) - q(M-x))\sqrt{\frac{w(x;q,M)}{\rho(1;q,M)}}, \tag{18}$$

where

$$\alpha_m = (x+1-m-q(M-2m+2))\sqrt{\frac{m}{q(1-q)(M-m+1)}}, \tag{19}$$

$$\beta_m = q(1-q)(M-m+2)\sqrt{\frac{m(m-1)}{(q(1-q))^2(M-m+2)(M-m+1)}}. \tag{20}$$

Note that the weighted Krawtchouk polynomials defined in Eq. (12) are orthogonal in one-dimensional signals. They can also be extended to apply to two-dimensional signals. Consider a 2-D signal image $g(x,y)$ defined on the discrete space $\{1,2,\dots,M\} \times \{1,2,\dots,N\}$. The following new set is orthogonal in the 2-D signal $g(x,y)$:

$$\{\widetilde{K}_m(x;q_x,M).\widetilde{K}_n(y;q_y,N): m = 1\dots,M, n = 1,\dots,N\}. \tag{21}$$

These new set of polynomials, as given in Eq. (12), satisfy the orthogonality condition:

$$\sum_{x=1}^{M}\sum_{y=1}^{N}\widetilde{K}_m(x;q_x,M)\widetilde{K}_n(y;q_y,N).\ \widetilde{K}_{m'}(x;q_x,M)\ \widetilde{K}_{n'}(y;q_y,N) = \delta_{mm'}\,\delta_{mm'} \tag{22}$$

The moments Q_{mn} of order $(m+n)$ of the image function $g(x,y)$ represent the projection of $g(x,y)$ onto the weighted Krawtchouk polynomials.

These moments are defined by:

$$Q_{mn} = \sum_{x=1}^{M}\sum_{y=1}^{N} g(x,y).\widetilde{K}_m(x;q_x,M)\widetilde{K}_n(y;q_y,N). \tag{23}$$

Now, by utilizing the orthogonal property in Eq. (22) and solving Eq. (23) for $g(x,y)$, the 2-D image function $g(x,y)$ can be reconstructed in terms of the Krawtchouk moments as:

$$g(x,y) = \sum_{m=1}^{M}\sum_{n=1}^{N} Q_{mn}.\widetilde{K}_m(x;q_x,M)\widetilde{K}_n(y;q_y,N). \tag{24}$$

Given a color image $g(x,y,z)$, where (x,y) are the spatial coordinates, and $z = 1,2,3$ represents the three channels (red, green, blue) of this color image, our goal is to reconstruct $g(x,y,z)$ using weighted discrete Krawtchouk polynomials. The proposed reconstruction approach is carried out through three algorithms:

1. Calculating Krawtchouk moments for $g(x,y,i), i = 1,2,3$.
2. Computing Krawtchouk is the inverse for every channel.
3. Reconstruction operations.

3.2. Color Image Watermarking in Transformed Domain

Transformed domains, such as discrete cosine transform, discrete Fourier transform, wavelet transform, and moments transform, find widespread application in various image processing domains, including image encryption [50], medical images [2], and image watermarking [51]. In this section, we propose a novel color image watermarking scheme based on the moment transform using weighted Krawtchouk polynomials introduced in above section. Transform domain techniques have gained considerable attention due to their robustness against image attacks like filtering, noise, compression, and geometric distortions, unlike spatial-based domain techniques.

Furthermore, the utilization of orthogonal Krawtchouk moments in our proposed image watermarking algorithm ensures robust watermark embedding, leveraging their inherent resilience. The proposed image watermarking technique comprises four primary stages: preprocessing, embedding procedure, extraction procedure, and watermarking evaluation.

Preprocessing Stage: During this stage, adjustments are made to the sizes of both the host and watermark images to enable the division of the host image into a whole number of blocks. Additionally, the watermark image is converted into a binary image. The preprocessing stage can be summarized through the following steps:

1. Input the color host image ($host\_C$) and watermark image (W).
2. Resize $host\_C$ to 512×512 pixels.
3. Resize W to 64×64 pixels.
4. Extract the three-color channels ($host\_R, host\_G, and\ host\_B$) from $host\_C$.
5. Convert the watermark image W into a binary image $W1$.

Embedding Procedure: In this stage, the three host channels, namely $host\_R, host\_G, and\ host\_B$, along with the binary watermark image $W1$, are received from the preprocessing stage. The host image's channels are divided into non-overlapping blocks, and the Krawtchouk moment transforms in Algorithm 1 is applied to each block. This entails determining parameters such as the block size, the maximum number of blocks, and the embedding parameter. The inverse Krawtchouk transform in Algorithm 2 is applied on the modified blocks at the end of procedure. The embedding of watermark $W1$ into the three host channels is summarized in the following procedure:

Algorithm 1: Krawtchouk Moments via its recurrence relations

INPUT: *One channel image* $g(x,y,i), i = 1,2,3$, *Krawtchouk parameters* $q_x, q_y \in (0,1)$, *moment order (m+n).*

OUTPUT: *Image moments* Q_{mn}^{i} *for channel i.*

$[M,N] = size(g(x,y,i));$

Define the horizontal vector $x = (1, \dots, M)$.

Define the vertical vector $y = (1, \dots, N)^t$.

Compute $\widetilde{K}_0(x; q_x, M)$ *using initial formula in (17):*

$$\widetilde{K}_0(x; q_x, M) = sqrt(KrawW(x; q_x, M)/\rho(0; q_x, M)).$$

Compute $\widetilde{K}_1(x; q_x, M)$ *using initial formula in (18):*

$$\widetilde{K}_1(x; q_x, M) = (x(1-q_x) - q_x(M-x)) \times sqrt(KrawW(x; q_x, M)/\rho(1; q_x, M)).$$

for *m=2 to M* **do**

$$\alpha_m = \left(x + 1 - m - q_x(M - 2m + 2)\right) \times sqrt(m/(q_x(1-q_x)(M-m+1))).$$

$$\beta_m = q_x(1-q_x)(M-m+2) \times sqrt((m(m-1))/((q_x(1-q_x))^2(M-m+2)(M-m+1))).$$

$$\widetilde{K}_m(x; q_x, M) = \alpha_m \widetilde{K}_{m-1}(x; q_x, M)/m - \beta_m \widetilde{K}_{m-2}(x; q_x, M)/m.$$

end for

Compute $\widetilde{K}_0(y; q_y, N)$ *as in step 6.*

Compute $\widetilde{K}_1(y; q_y, N)$ *as in step 7.*

for *n=2 to N* **do**

$$\alpha_n = \left(y + 1 - n - q_y(N - 2n + 2)\right) \times sqrt(n/(q_y(1-q_y)(N-n+1))).$$

$$\beta_n = q_y(1-q_y)(N-n+2) \times sqrt((n(n-1))/((q_y(1-q_y))^2(N-n+2)(N-n+1))).$$

$$\widetilde{K}_n(y; q_y, N) = \alpha_n \widetilde{K}_{n-1}(y; q_y, N)/n - \beta_n \widetilde{K}_{n-2}(y; q_y, N)/n.$$

end for

$$Q_{mn}^{i} = \widetilde{K}_m^t(x; q_x, M) \times g(x,y,i) \times \widetilde{K}_n(y; q_y, N).$$

Return *the moments* Q_{mn}^{i}.

Algorithm 2: Krawtchouk inverse for one-channel image

INPUT: *Image moment* Q_{mn}^{i} *received from algorithm 1.*
OUTPUT: *An approximated reconstruction* $\hat{g}(x,y,i)$ *of one-channel image* $g(x,y,i)$.
Get the dimensions [M, N] of Q_{mn}.
Define the horizontal vector $x = (1,\dots,M)$.
Define the vertical vector $y = (1,\dots,N)^t$.
Compute Krawtchouk polynomials $\widetilde{K}_m(x;q_x,M)$ *for vector x using algorithm 1.*
Compute Krawtchouk polynomials $\widetilde{K}_n(y;q_y,N)$ *for vector y using algorithm 1.*
$\hat{g}(x,y,i) = \widetilde{K}_m(x;q_x,M) \times Q_{mn}^{i} \times \left(\widetilde{K}_n(y;q_y,N)\right)^t$.
Return the *approximated reconstruction* $\hat{g}(x,y,i)$.

Algorithm 3: Reconstruction operations of color image using Krawtchouk polynomials

INPUT: *Original color image* $g(x,y,i)$ *for* $i = 1,2,3$ *(representing the color channels), Krawtchouk parameters* q_x, q_y, *moment order (m+n).*
OUTPUT: *Reconstructed color image* $(\hat{g}(x,y,i))$
Extract the three color channels: $g(x,y,1), g(x,y,2), g(x,y,3)$ *from* $g(x,y,i)$.
Get the dimensions [M, N] of $g(x,y,1)$.
Define the horizontal vector $x = (1,\dots,N)$.
Define the vertical vector $y = (1,\dots,M)^t$.
Compute Krawtchouk polynomials $\widetilde{K}_m(x;q_x,M)$ *for vector x using algorithm 1.*
Compute Krawtchouk polynomials $\widetilde{K}_n(y;q_y,N)$ *for vector y using algorithm 1.*
Calculate the Krawtchouk moments (Q_{mn}^{r}) *for the red channel* $g(x,y,1)$ *using algorithm 1.*
Calculate the Krawtchouk moments (Q_{mn}^{g}) *for the green channel* $g(x,y,2)$ *using algorithm 1.*
Calculate the Krawtchouk moments (Q_{mn}^{b}) *for the blue channel* $g(x,y,3)$ *using algorithm 1.*
Compute the approximated reconstruction $\hat{g}(x,y,1)$ *for the red channel using algorithm 2.*
Compute approximated reconstruction $\hat{g}(x,y,2)$ *for the green channel using algorithm 2.*
Compute approximated reconstruction $\hat{g}(x,y,3)$ *for the blue channel using algorithm 2.*
Build the reconstructed color image $\hat{g}(x,y,z)$ *using its individual components:* $\hat{g}(x,y,1)$, $\hat{g}(x,y,2)$, *and* $\hat{g}(x,y,3)$.

Extraction Procedure: To extract watermark $W2$ from the obtained watermarked image $host\_W$, the original host color image $host\_C$ is employed. The correlation coefficient between Krawtchouk moments in $host\_C$ blocks and their corresponding blocks in $host\_W$ is utilized to establish a threshold T. The value of $W2$'s pixel is then determined based on the threshold T. Procedure 2 summarizes the steps for extracting watermark $W2$.

Evaluation Stage: In the final stage, the performance of the proposed image watermarking approach is evaluated using four key measures. Two of these measures assess the quality of the watermarked image: the peak signal-to-noise ratio ($PSNR$) (Eq. 25) and the structural similarity index measurement ($SSIM$) (Eq. 27).

The remaining two measures are employed to evaluate the watermark's robustness: the bit error rate (BER) (Eq. 28) and the normalized cross-correlation (NCC) (Eq. 29). The values of these measures provide insights into the effectiveness of the image watermarking algorithm. When the $PSNR$ value exceeds 37 and the $SSIM$ value is close to unity, it indicates the watermark image's quality is favorable. On the other hand, a BER value close to zero and NCC value near one suggest a high level of algorithmic robustness. The subsequent steps outline how these watermark measures are computed.

Procedure 1: Embedding a binary watermark image in a host color image

INPUT: *host_R, host_G, host_B, and W1 received form preprocessing stage, embedding parameter α.*
OUTPUT: *Watermarked color image host_W.*
Calculate the dimensions [M, N] of host_R.
Determine the dimensions [m, n] of W1.
Calculate the block size using block_size = M/m.
*Compute the total number of blocks as block_num = (M * N) / block_size^2.*
Divide host_R, host_G, and host_B into block_num non-overlapping blocks.
Apply the Krawtchouk moment transform in Algorithm 1 to all blocks obtained in step 7.
***For** i = 1 **to** m*
  For *j = 1* **to** *n*
    If *(W1(i, j) == 1)*
      Modify block_R by adding (α × block_R).
      Modify block_G by adding (α × block_G).
      Modify block_B by adding (α × block_B).
    Else
      Modify block_R by subtracting (α × block_R).
      Modify block_G by subtracting (α × block_G).
      Modify block_B by subtracting (α × block_B).
    End *// if*
  End *// for j*
End *// for i*
Apply the Krawtchouk inverse in Algorithm 2 to all modified blocks from steps 12 and 18.
Construct the watermarked color image host_W using the modified channels host_R, host_G, and host_B.

Procedure 2: Extracting the embedded watermark image from the watermarked image

INPUT: *host_W, host_C, block_num, and embedding parameter α.*
OUTPUT: *Retrieved watermark W2.*
Extract host_R1 from host_W and host_R2 from host_C.
Divide host_R1 and host_R2 into block_num non-overlapping blocks.
Apply the Krawtchouk moment transform in Algorithm 1 to all blocks obtained in step 4.
Calculate the difference (diff) between corresponding blocks in host_R1 and host_R2.
Compute the normalized cross-correlation (NCC) between diff and block_R2.
Determine the threshold T = α × NCC.
For *i = 1* **to** *m*
  For *j = 1* **to** *n*
    If *(NCC > T)*
      Set W2(i, j) = 1.
    Else
      Set W2(i, j) = 0.
    End *// if*
  End *// for j*
End *// for i*
Return *W2.*

4. EXPERIMENTAL RESULTS

This section is divided into three subsections where many experiments are carried out to validate the theoretical proposed in section 2. The first subsection is dedicated to describe the used dataset which consists of 89 retina medical image established by Kauppi et al. [38]. In

the second subsection, the proposed technique for retina image reconstruction is verified. And comparisons with two continuous and two discrete moments are introduced to show the performance for each one in terms of $PSNR$ and MSE, and running time. In the third subsection, we provide extensive experimental studies of the proposed method implemented in watermarking application and analyze the attack effects on the retina medical image dataset. A comparison with state-of-the-art methods and widely used watermarking application is provided to show the improvement in $PSNR$, $SSIM$, BER, and NCC measures.

Procedure 3: Image watermarking Evaluation

INPUT: *the color host image* $host\_C$, *the watermarked image* $host\_W$, *the embedded watermark* $W1$, *and the extracted watermark* $W2$.
OUTPUT: $PSNR, SSIM, BER$, *and* NCC.
Extract the three channels $host\_R1, host\_G1$, *and* $host\_B1$ *from* $host\_C$.
Extract the three channels $host\_R2, host\_G2$, *and* $host\_B2$ *from* $host\_W$.
Compute PSNR using Eqs. 25 and 26, where $host\_C = f(x_i, y_j, z)$ *and* $host\_W = \hat{f}(x_i, y_{j,}, z)$.
Compute $SSIM1$ *between* $host\_R1$ *and* $host\_R2$ *using Eq. 27.*
Compute $SSIM2$ *between* $host\_G1$ *and* $host\_G2$ *using Eq. 27.*
Compute $SSIM3$ *between* $host\_B1$ *and* $host\_B2$ *using Eq. 27.*
Calculate the SSIM between $host\_C$ *and* $host\_W$ *as the average of* $SSIM1$, $SSIM2$, *and* $SSIM3$.
Compute BER *between* $W1$ *and* $W2$ *using Eq. 28.*
Compute NCC *between* $W1$ *and* $W2$ *using Eq. 29.*
Return *the computed values of PSNR, SSIM, BER, and NCC.*

4.1. Dataset Description

A necessary tool for performance evaluation and comparisons of reconstruction and watermarking algorithms is a dataset of selected high-quality retina medical images which are representatives of the interested problem and have been verified by experts such as Diabetic Retinopathy Dataset DIARETDB [38]. In the following, we describe the images of DIARETDB database which taken in the Kuopio university hospital, Finland. The DIARETDB database consists of 89 multi-channel fundus images of size 1500×1152 five of them are normal which do not contain any marks of the diabetic retinopathy (an example shown in Fig. 1(a), and the remaining 84 images are abnormal which contain at least mild no proliferative marks of the diabetic retinopathy (2 examples shown in Figs. 1(b and c).

(a) (b) (c)

Fig. 1. Examples of DIARETDB multi-channel fundus images: a) normal; b) abnormal; and c) abnormal after treatment by photocoagulation.

The abnormalities in the database images are relatively small, but they appear near the macula and this is considered to threaten the vision. The images were captured with the same digital fundus camera with 50-degree field-of-view and varying imaging settings such as flash intensity and shutter speed. Therefore, the images contain an amount of imaging noises. The optical aberrations (dispersion or field curvature) and the photometric accuracy (intensity or color) are the same, therefore, the photometric variance over the visual appearance can be considered as small.

4.2. Retina Image Reconstruction

In image analysis, image reconstruction is the inverse process of computing orthogonal moments. In the context of medical images, this process is employed to assess the accuracy of computed orthogonal moments. To evaluate the reconstruction process, we compare the proposed multi-channel reconstruction algorithm with two continuous orthogonal moments: Radial Harmonic Fourier Moments (RHFM) [39] and Exponent-Fourier Moments (EFM) [40], as well as two discrete orthogonal moments: Charlier [41] and Tchebichef [42]. Figure 2 illustrates the reconstructed DRMI image based on the image in Fig. 1(a) using various moment orders and the compared methods, along with the proposed reconstruction method. Notably, the images reconstructed by continuous methods exhibit a circular artifact in the center and are degraded by the two discrete methods compared. Conversely, the proposed method yields the best results, with the reconstructed image closely resembling the original one. In the evaluation of reconstructed image quality, $PSNR$ and MSE are commonly used metrics in the medical image processing community. A precise reconstruction algorithm should take the DRMI image as input and generate an output image with a maximum $PSNR$ and a minimum MSE. For a DRMI image represented as $f(x, y, z)$ with dimensions of $m \times n \times 3$ pixels, $PSNR$ and MSE are defined as:

$$PSNR = 10 \times \log_{10}\left(\frac{f_{max}^2}{MSE}\right), \tag{25}$$

$$MSE = \frac{1}{3(m \times n)} \sum_{z=1}^{3} \sum_{i=1}^{m} \sum_{j=1}^{n} \left(f(x_i, y_j, z) - \hat{f}(x_i, y_{j,}, z)\right)^2. \tag{26}$$

where $\hat{f}(x_i, y_j, z)$ is the reconstructed image. For the continuous moments RHFM [39] and EFM [40] the error in Eq. (26) is given because of the discrete approximations while the same error for discrete moments Chariler [41] and Tchebichef [42] using finite number of moments. The proposed reconstruction algorithm overcomes these problems by using the orthogonal Krawtchouk moments with parameters 0.5 and 0.5 where the MSE decrease quickly as moment order increases. Consequently, the reconstructed image will be very close to the original one when the moment order reaches a certain value.

To test the accuracy of the reconstruction process for the methods considered, a variety of images from the DIARETDB dataset were selected. Samples of these images are displayed in Fig. 1. Both $PSNR$ and MSE were computed using two continuous moments, two discrete moments, and the proposed reconstruction algorithm. The graphical representation of $PSNR$ values for the five methods is depicted in Fig. 3 for easier comparison. The $PSNR$ of the proposed method monotonically increased with an increasing moment order, while the Charlier moment method showed slow improvement, and the Tchebichef moment method significantly degraded when the moment order exceeded 120 due to numerical instabilities. In contrast, the $PSNR$ of the two continuous methods remained approximately constant with insignificant increases as the moment order increased. To evaluate the performance of the

proposed reconstruction method in terms of MSE, another random sample from the DIARETDB dataset was selected. The MSE values of the compared methods and the proposed method were computed and summarized in Table 1. The results in this Table reveal that the image reconstruction errors of the proposed method are very small compared to the errors obtained by the two discrete methods and the two continuous methods, especially when the moment order exceeds 120. The Tchebichef method exhibits the highest error when the moment order is greater than or equal to 160. The continuous methods have approximately the same MSE, which is greater than the error of the proposed method when the moment order is greater than or equal to 120. These results confirm that the accuracy of the proposed reconstruction method surpasses that of the other methods when the moment order is greater than or equal to 120.

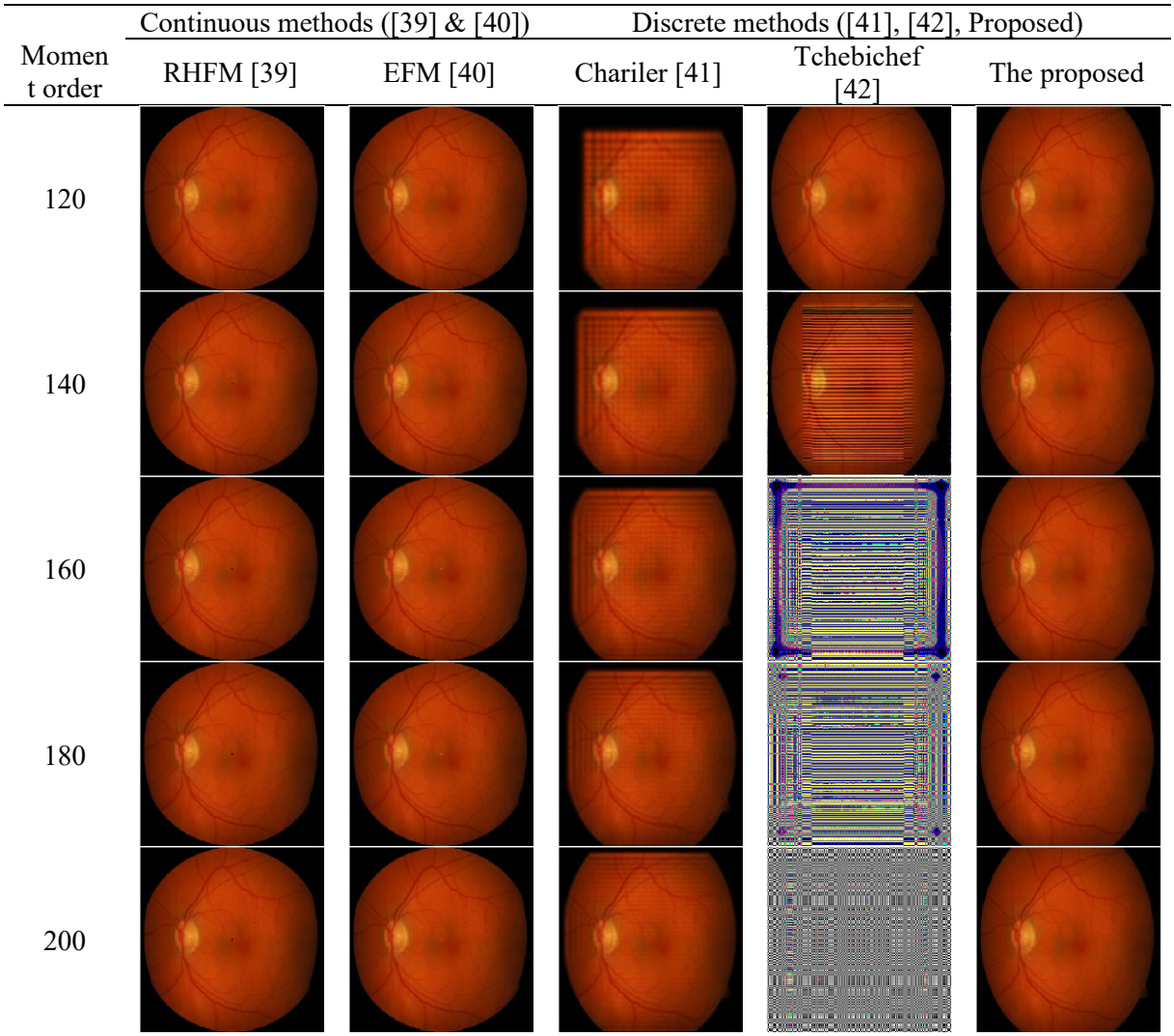

Fig. 2. Some samples of reconstructed DRMI images from the DIARETDB database at different values of moment order using the compared methods and the proposed.

The influence of noise on any new technique is a crucial aspect to evaluate. To assess the robustness of the proposed reconstruction technique against the adverse effects of certain types of noise, we introduced 'salt & pepper' and 'white Gaussian' noise to the original DRMI images. The noise-free DRMI image and its versions contaminated with 'salt & pepper' and 'white Gaussian' noise are displayed in Figs. 4(a, b, c). These two types of noise were added to the original DRMI image using the following MATLAB instructions:

$$f = imnoise(f, 'salt \ \& \ peppers', a)$$
$$f = imnoise(f, 'Gaussian', b, c)$$

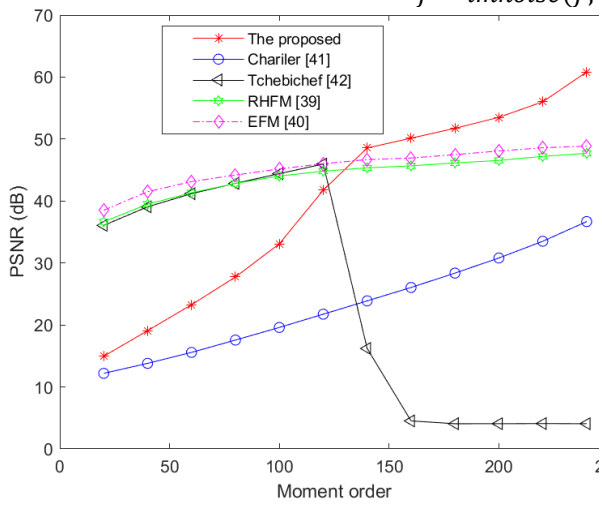

Fig. 3. Average PSNR of 20 DRMI images randomly selected from The DIARETDB dataset at different orders.

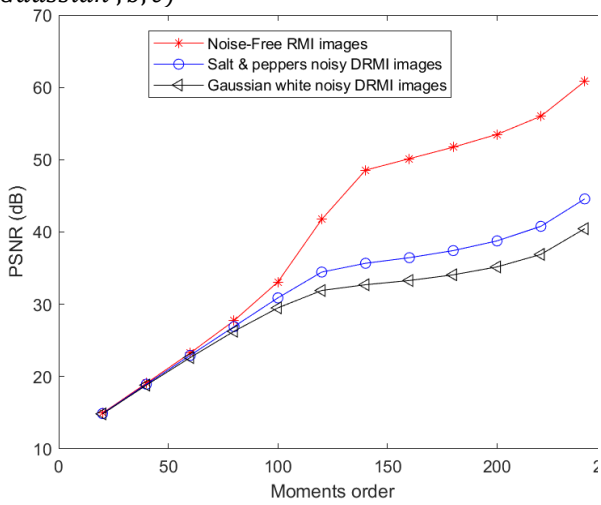

Fig. 4. Average PSNR of 20 DRMI images exposed to two different types of noise using the proposed reconstruction method.

Table 1. The average MSE values for the reconstruction process by using RHFM [39], EFM [40], Chariler [41], Tchebichef [42], and the proposed reconstruction algorithm.

	Moments order											
	20	40	60	80	100	120	140	160	180	200	220	240
[39]	0.0036	0.0017	0.001	7.3 E-4	5.5 E-4	4.6 E-4	4.0 E-4	3.8 E-4	3.4 E-4	3.1 E-4	2.6 E-4	2.4 E-4
[40]	0.0021	0.001	6.8 E-4	5.3 E-4	4.2 E-4	3.4 E-4	2.9 E-4	2.8 E-4	2.54 E-4	2.2 E-4	1.9 E-4	1.8 E-4
[41]	0.8442	0.5820	0.3874	0.2449	0.1533	0.0937	0.0571	0.0347	0.0203	0.011	0.006	0.003
[42]	0.0034	0.0017	0.0010	0.0007	0.0005	0.0003	0.3345	4.9410	5.4848	5.478	5.452	5.477
Prop.	0.4475	0.1724	0.0659	0.0235	0.0068	0.0009	0.0001	0.0001	9.3E-5	6.2 E-5	3.5 E-5	1.1 E-5

Here, the numerical parameters a, b, and c were used to control the noise density in the image. The noise-contaminated images and the original noise-free image were reconstructed using the proposed reconstruction method with moment orders ranging from 20 to 240. The plotted $PSNR$ curves for these images are displayed in Fig. 5.

It is evident that the $PSNR$ values of noisy DRMI images are smaller than their corresponding $PSNR$ values of the noise-free image.

(a) **(b)** **(c)**

Fig. 5. Example of DRMI image and its contaminated version: a) noise-free DRMI image; b) noisy DRMI image: Salt & Peppers, and c) noisy DRMI image: white Gaussian.

As depicted in Fig. 5, the $PSNR$ curves of the noise-contaminated images increased as the moment order increased. The $PSNR$ values for contaminated images exceeded 30 when the moment order was greater than 100. These observations confirm the robustness of the proposed reconstruction method against different types of noise. Computation cost is a critical concern in medical image reconstruction. We will compare the CPU running time required for reconstructing DRMI images using the five different methods. The average CPU running times for image reconstruction of resized DRMI images (256×256) are displayed in Fig. 6 and Fig. 7. Due to the significant difference in the scale of CPU running times required by continuous and discrete methods, Fig. 6 presents only the continuous methods RHFM [39] and EFM [40], while Fig. 7 includes the discrete methods Charlier [41], Tchebichef [42], and the proposed reconstruction method. It is evident from Fig. 6 that both RHFM [39] and EFM [40] consume a substantial amount of running time, rendering them impractical for real-world applications. In contrast, the discrete methods shown in Fig. 7 significantly reduce the computational time, particularly the proposed method. These comparisons underscore the superiority of our technique in terms of running time.

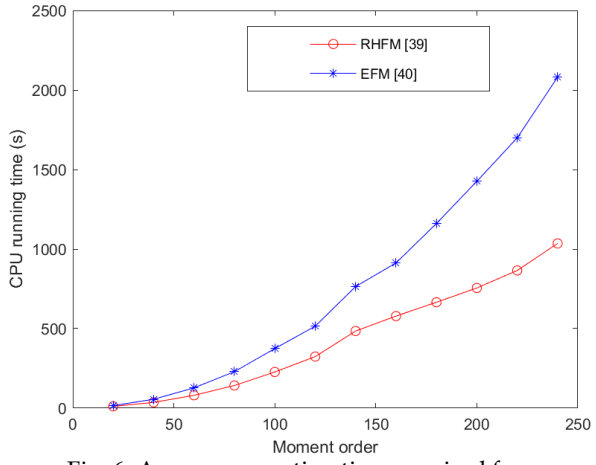

Fig. 6. Average execution time required for reconstructing DRMI images using RHFM [39] and EFM [40].

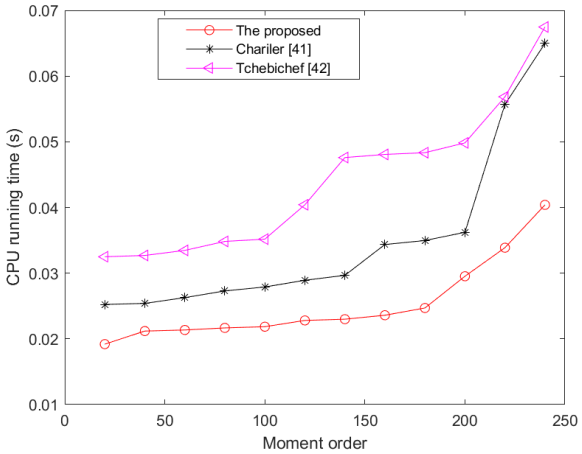

Fig. 7. Average execution time required for reconstructing DRMI images using Chariler [41], Tchebichef [42], and the proposed reconstruction method.

4.3. Retina Image Watermarking

4.3.1. Embedding Parameter Effect

In the first watermarking experiment, the embedding parameter effect was tested through the watermarking insertion process in the host DRMI image. Using the all 89 DRMI images from the DIARETDB dataset and the 4 binary chicken images of size 64 × 64 is used as the watermarks, 356 host image and watermark pairs are generated. A sample from the DIARETDB dataset used as a host image are shown in Fig. 8. Four binary chicken images taken with different angles used as watermark images are displayed in Fig. 9. For each image pair (host, watermark), the chicken watermark is embedded in the DRMI image with Krawtchouk parameters $q_x = q_y = 0.5$ and the embedding parameter step is increasing from 0.01 to 0.1 with an increment equal to 0.01. Figure 10 shows the effect of the embedding parameter by displaying visually the image 001 after embedding the watermark image in Fig. 9(a) using different values of the embedding parameter α. It can be observed that when $= 0.02$, the watermark is invisible and when α is greater than or equal 0.04, the watermark gradually

becomes visible. The $PSNR$ values between the original image and the watermarked image are calculated. Figure 11 displays the average $PSNR$ values of the 356 watermarked images for the embedding parameter steps. It can be observed from Fig. 11 that the $PSNR$ value of the watermarked image decreases with the increase of the embedding parameter α. A larger embedding parameter step is required for best robustness, meanwhile the quality of watermarked image deteriorates. To get a watermark invisible, the $PSNR$ value is expected to be greater than 40 dB. Therefore, the embedding parameter step of the proposed scheme could be selected to 0.02, leading to an average $PSNR$ value of 45.39 dB.

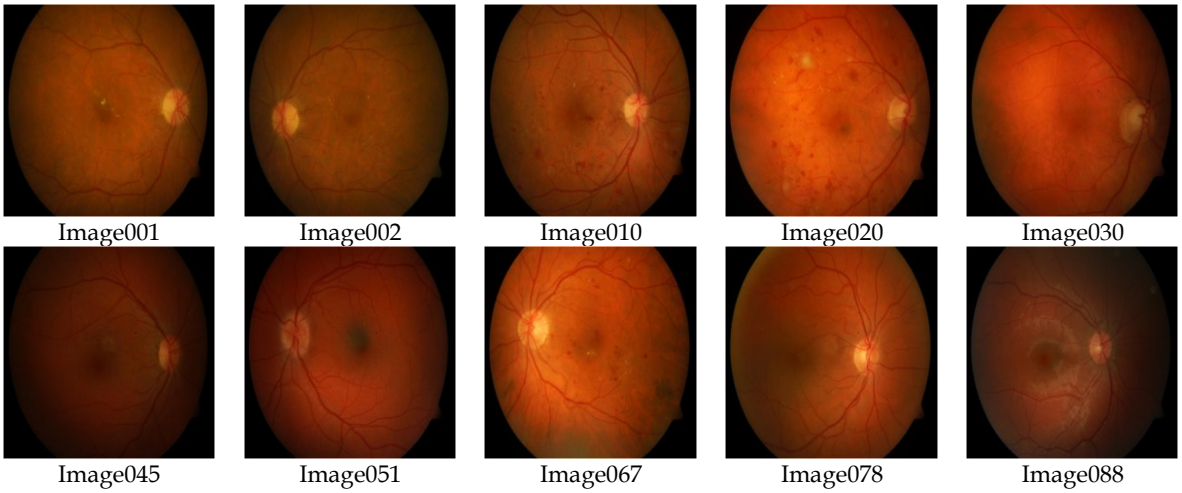

Fig. 8. Example from ten images selected from the DIARETDB dataset.

(a) Binary watermark (b) Watermark in (a) rotated by 90. (c) Watermark in (a) rotated by 180. (d) Watermark in (a) rotated by 270.

Fig. 9. Binary watermark image with different angles.

Fig. 10. Embedding parameter effect showing on image001 and watermark in Fig. 9(a)

4.3.2. Imperceptibility quality analysis

The imperceptibility quality is examined for both the watermarked image and the retrieved watermark. For the watermarked DRMI image the $PSNR$ measure in Eq. 25 is used to measure the visual quality and the $SSIM$ measure that reflect image degradation change in structural information is computed between host DRMI image h and watermarked image w as:

$$SSIM(h,w) = \frac{(2\mu_h\mu_w+C_1)(2\sigma_{hw}+C_2)}{(\mu_h^2+\mu_w^2+C_1)(\sigma_h^2+\sigma_w^2+C_2)} \quad (27)$$

where $\mu_h$and μ_w are the average intensities of images h and w, respectively, while σ_h^2 and σ_w^2 are the corresponding variances. σ_{PE} refers to the covariance between h and w, while C_1 and

C_2 are constants. $SSIM(h,w) = 1$ means that h and w are identical and $SSIM(h,w) < 1$ indicate that h and w are different.

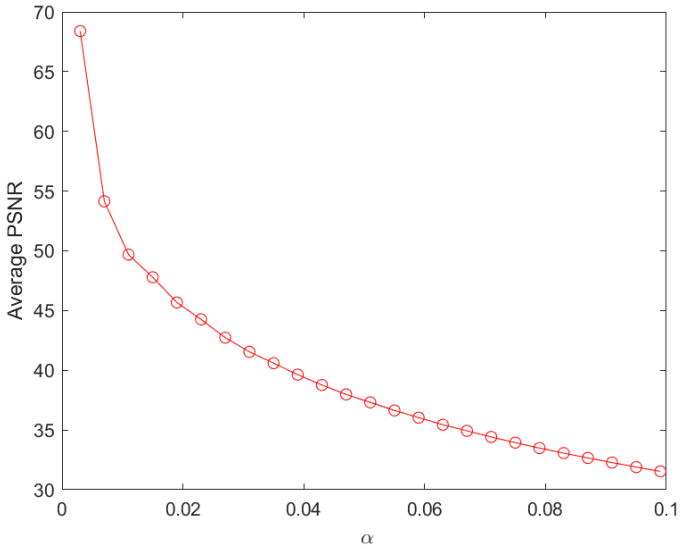

Fig. 11. Average PSNR values taken over DIARETDB dataset depending on the watermark embedding parameter α.

Methods	Cox *et al.* [43]	Ko *et al.* [44]	Fares *et al.* [45]	Liu *et al.* [46]	The Proposed
Watermarked DRMI image					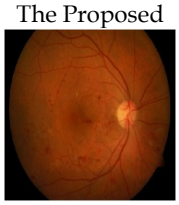
$PSNR$	40.4121	42.9965	43.8054	56.6259	44.8822
$SSIM$	0.9745	0.9830	0.9931	0.9998	0.9996
Retrieved watermark					
BER	0.2542	0.0393	0.0552	0.1016	0.0024
NCC	0.773796	0.9932	0.9725	0.8590	0.9968

Fig. 12. A visual representation and quantitative assessment of the watermarked DRMI image010, the quality metrics ($PSNR$ and $SSIM$), and the retrieved watermark (chicken image) along with its evaluation metrics (BER and NCC).

On the other hand, the quality of the retrieved watermark is evaluated using BER and NCC measures. The $BER(w, w_1)$ between the input watermark w and retrieved watermark w_1 is the proportion of number false extracted bits in w_1 to the total number of watermark bits in w and defined by the relation:

$$BER(w, w_1) = \frac{1}{m \times n} \sum_{i=1}^{m} \sum_{j=1}^{n} (w(i,j) \oplus w_1(i,j)) \tag{28}$$

The value of $BER(w, w_1)$ close to zero indicates a more robust technique. The last measure $NCC(w, w_1)$ is a statistical measure used to evaluate the similarity degree between input watermark w and the retrieved watermark w_1 and expressed mathematically as:

$$NCC(w, w_1) = \frac{\sum_{i=1}^{m} \sum_{j=1}^{n} (w(i,j) \times w_1(i,j))}{\sqrt{\sum_{i=1}^{m} \sum_{j=1}^{n} w^2(i,j)} \sqrt{\sum_{i=1}^{m} \sum_{j=1}^{n} w_1^2(i,j)}} \tag{29}$$

The value of $NCC(w, w_1)$ close to one indicates a more similarity between the input watermark w and the retrieved watermark w_1.

The performance of the proposed watermarking method is evaluated using the above measures, $PSNR, SSIM, BER$ and NCC. To assess the effectiveness of the proposed watermarking method, a comparative analysis is conducted with four similar watermarking algorithms in the transform domain: Cox et al.'s algorithm (1997) [43], Liu et al.'s algorithm (2019) [46], Ko et al.'s algorithm (2020) [44], and Fares et al.'s algorithm (2020) [45]. By comparing the performance of the proposed method with these state-of-the-art approaches, we aim to provide a comprehensive evaluation of its effectiveness and superiority in watermarking multi-channel DRMI images. Figure 12 illustrates the results of embedding and extracting watermarks using the proposed method and the compared methods. In this experiment, no attacks were applied to the host image (image010 from Fig. 8) and the watermark image (Fig. 9(b)). The second row of the Figure displays the watermarked images generated by all methods, showing that all methods achieve high quality. This is evident from the $PSNR$ values, which are greater than 40 dB, and the $SSIM$ values, which exceed 0.9700. It is worth noting that both the proposed method and Liu et al. [46] demonstrate the best results. The fifth row of the Figure presents the retrieved watermark, while the sixth and seventh rows display the corresponding evaluation measures. Visual observation of the retrieved watermark in the fifth row confirms that the proposed method yields the best result. Additionally, the values of BER and NCC support this observation. The BER value is very close to zero (0.0024), indicating minimal errors, while the NCC value is nearly one (0.9968), suggesting a strong correlation between the retrieved and original watermarks.

In order to obtain fair and accurate results, the performance of the proposed watermarking method and the compared methods were tested on a random set comprising ten images. The average values of the four evaluation measures were computed for a comprehensive analysis. Figures 13 and 14 provide graphical comparisons of the watermarked image quality in terms of $PSNR$ and $SSIM$, respectively. These Figures offer visual insights into the performance of the methods.

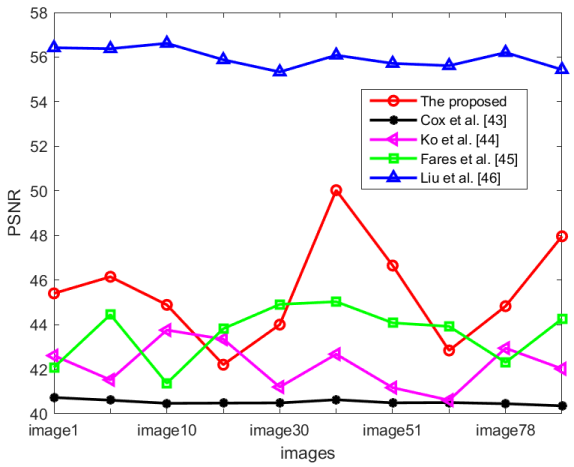

Fig. 13. $PSNR$ curves of the considered methods applied on the ten DRMI images in Fig. 8.

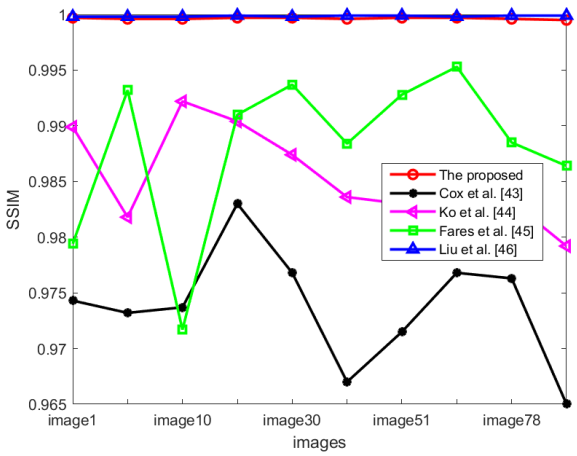

Fig. 14. $SSIM$ curves of the considered methods applied on the ten DRMI images in Fig. 8.

Figs. 15 and 16 present graphical comparisons of the robustness and similarity of the retrieved watermark using the measures of BER and NCC, respectively. These Figures illustrate the effectiveness of the methods in maintaining the integrity and accuracy of the retrieved watermarks. Furthermore, Table 2 presents the average values of the four evaluation measures calculated for the entire dataset. This Table provides a concise summary of the performance of each method across multiple images, allowing for a comprehensive understanding of their

capabilities. By conducting these evaluations and presenting the results through graphical comparisons and averaged values, a comprehensive assessment of the proposed watermarking method and the compared methods can be obtained, ensuring a more reliable and thorough analysis of their performance.

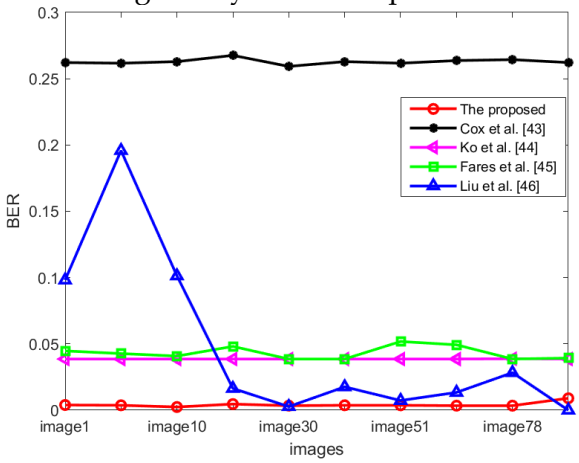

Fig. 15. BER curves of the considered methods applied on the ten DRMI images to extract the watermark image in Fig. 9(b).

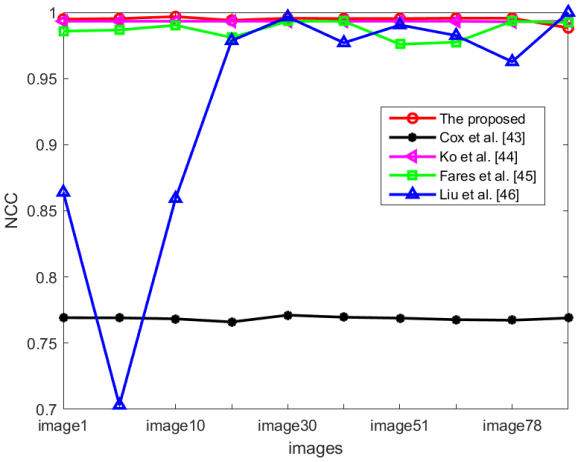

Fig. 16. NCC curves of the methods considered applied on the ten DRMI images to extract the watermark image in Fig. 9(b).

Table 2: The average values of the four evaluation measures computed for the entire dataset using the five methods considered.

	PSNR	*SSIM*	*BER*	*NCC*
Cox et al. [43]	40.5191	0.9737	0.2628	0.7686
Ko et al. [44]	42.1839	0.9853	0.0386	0.9932
Fares et al. [45]	43.6191	0.9880	0.0432	0.9869
Liu et al. [46]	**55.9684**	**0.9998**	0.0480	0.9314
The proposed	45.4931	**0.9996**	**0.0041**	**0.9946**

4.3.3. Watermarking capacity

The proposed watermarking algorithm embeds one bit of the watermark into each Krawtchouk transform block of the host DRMI image. In the watermarking experiments, the DRMI images were resized to 512×512, and they already have three channels. The embedded chicken watermark image has a size of 64×64. Therefore, a total of 12,288 bits can be embedded into the host DRMI image, calculated as $64 \times 64 \times 3$. Figure 17 depicts the capacity of the proposed algorithm in comparison with four existing watermarking algorithms. It can be seen that both the proposed algorithm and Sahabir et al. [48] offer a large capacity, whereas other algorithms demonstrate limited capacity for different reasons. For instance, in [47], the watermark embedding is limited to less correlated low and high frequency bands, while [49] embeds the watermark in the blocks of the image's luminance matrix, resulting in fewer blocks compared to embedding in the R, G, and B planes.

4.3.4. Watermarking Attacks

A watermarked image is susceptible to various types of attacks, which can be classified into four categories: Filter attacks, Geometric attacks, Noise attacks, and Robustness attacks. In Filter attacks, attackers apply different types of filters to watermarked images, compromising the effectiveness of watermarking techniques. Geometric attacks involve altering the geometry of the image by changing its translation, scaling, or rotation. Noise attacks entail the addition of different types of noise to degrade the quality and integrity of

watermarked images. Lastly, Robustness attacks involve attempts to remove the watermark through methods such as JPEG compression and cropping of the watermarked image.

In the attack experiments, we employ a series of twelve watermarking attacks to assess and compare the robustness of the proposed watermarking algorithm against related watermarking algorithms. Each attack is parameterized with three values, reflecting varying levels of impact low, medium, and high on the watermarked content. The impact of the attack on the watermarked image is assessed through the following steps: First, the watermarked image undergoes each attack using three distinct parameters, resulting in a set of attacked watermarked images. Subsequently, the watermark extraction procedure is applied to each attacked image. Finally, the BER and NCC measures are computed between the original and extracted watermark. This process is executed on a randomly selected set of ten samples from the dataset, utilizing the watermark depicted in Fig. 9(c).

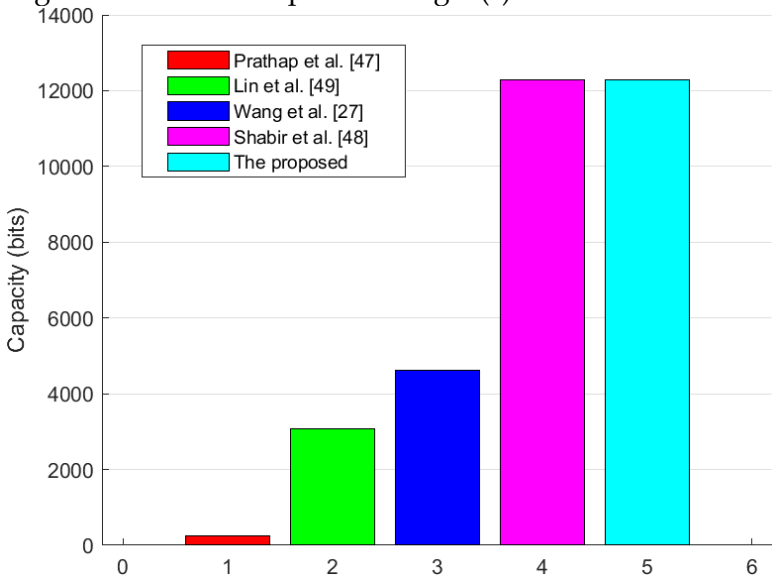

Fig. 17. Capacity comparison with related algorithms.

4.3.4.1. Filter Attacks

Filter attacks encompass a range of intentional manipulations aimed at compromising the effectiveness of watermarking techniques by applying various types of image filters to watermarked images. These attacks are designed to assess the robustness of watermarking methods against filtering operations that can distort or obscure the embedded watermark. Examples of such filtering operations encompass average filters, median filters, sharpening filters, and blurring filters (e.g., Gaussian blur).

Figure 18 visually presents the extracted watermarks along with their respective BER values for the five methods, following exposure to the average, median, blurring, and sharpening filters. Meanwhile, Fig. 19 offers a graphical comparison of the proposed algorithm's performance against other techniques when subjected to the same attacks. It is evident from the Figs. (18(a, b, c) and 19(a, b, c)) that the proposed method demonstrates greater robustness than other methods against average, median, and blurring attacks. Notably, the median filter attack achieves the lowest BER value (0.0095). While, Ko et al. [44] exhibits greater robustness than the proposed technique and other methods in terms of the sharpening attack, as shown in Figs. 18(d) and 19(d).

4.3.4.2. Geometric Attacks

Geometric attacks encompass a range of deliberate manipulations and transformations applied to watermarked images with the intent to undermine the effectiveness of the embedded watermark. These attacks primarily focus on the spatial attributes of the watermark, involving alterations to its size, orientation, or position. To evaluate the methods'

robustness, three types of geometric attacks – scaling, rotations, and shifting – are applied to the watermark image.

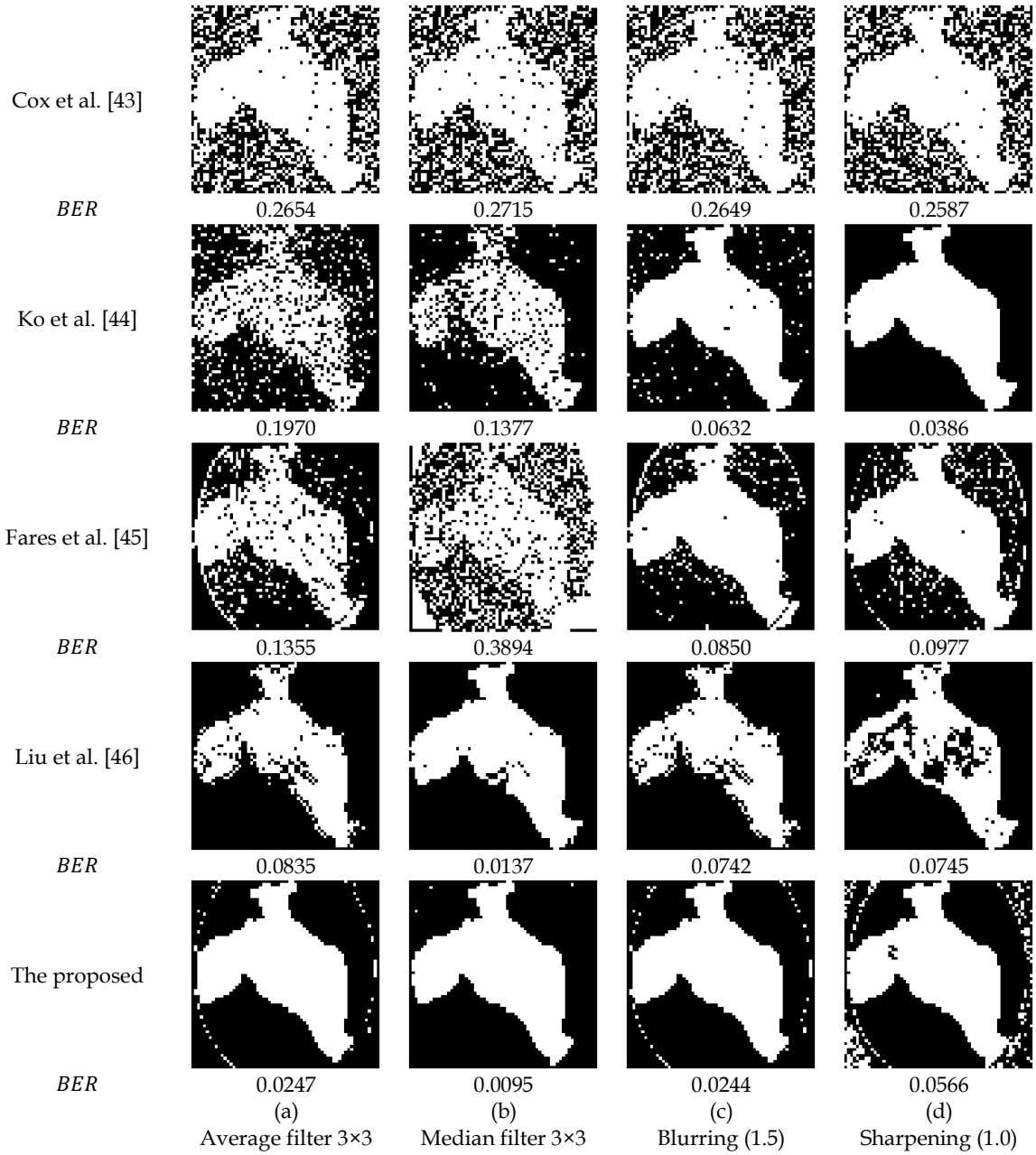

Fig. 18. Visual outcomes of the extracted watermarks using the proposed technique and the compared methods under filter attacks.

In the first geometric attack, scaling, the watermarked image is resized by different scales. To extract the watermark from the scaled images, the watermarked images are subsequently resized back to the original size. Figure 20(a) displays the extracted watermark from the watermarked image after being resized by half (50%) using the five methods. It is evident that both Liu et al. [46] and the proposed method effectively recognize the watermark more than the other three methods. This is further substantiated graphically by Fig. 21(a), where the performance of Liu et al. [46] and the proposed method yield results in a lower BER for scaling of 50%, 75%, 150%, and 200%. In the second geometric attack, rotation, the watermarked image is rotated by various angles in the clockwise direction. To extract the watermark from the rotated images, the watermarked images are subsequently re-rotated

counterclockwise to restore the pixels to their original positions. Figure 20(b) displays the extracted watermark from the watermarked image after a 30-degree rotation using the five methods. It is evident that the proposed method effectively recognizes the watermark more than the other methods. This is further supported graphically by Fig. 21(b), where the performance of the proposed method results in a lower BER for rotations of 30^{o}, 60^{o}, and 80^{o} degrees. In the final geometric attack, known as shifting, the watermarked image undergoes a horizontal transformation achieved by moving the camera linearly by a certain number of pixels. The watermark is subsequently extracted for three distinct horizontal motion values. Figure 20(c) displays the visual outcomes obtained using the five methods after applying a horizontal shift of 10 pixels, while Fig. 21(c) presents a comparative analysis of the methods across three different shift values. It is evident that the proposed method exhibits superior performance in watermark recognition, with the lowest BER. Furthermore, the proposed method outperforms the others when the watermark image is shifted by 10, 50, and 100 pixels.

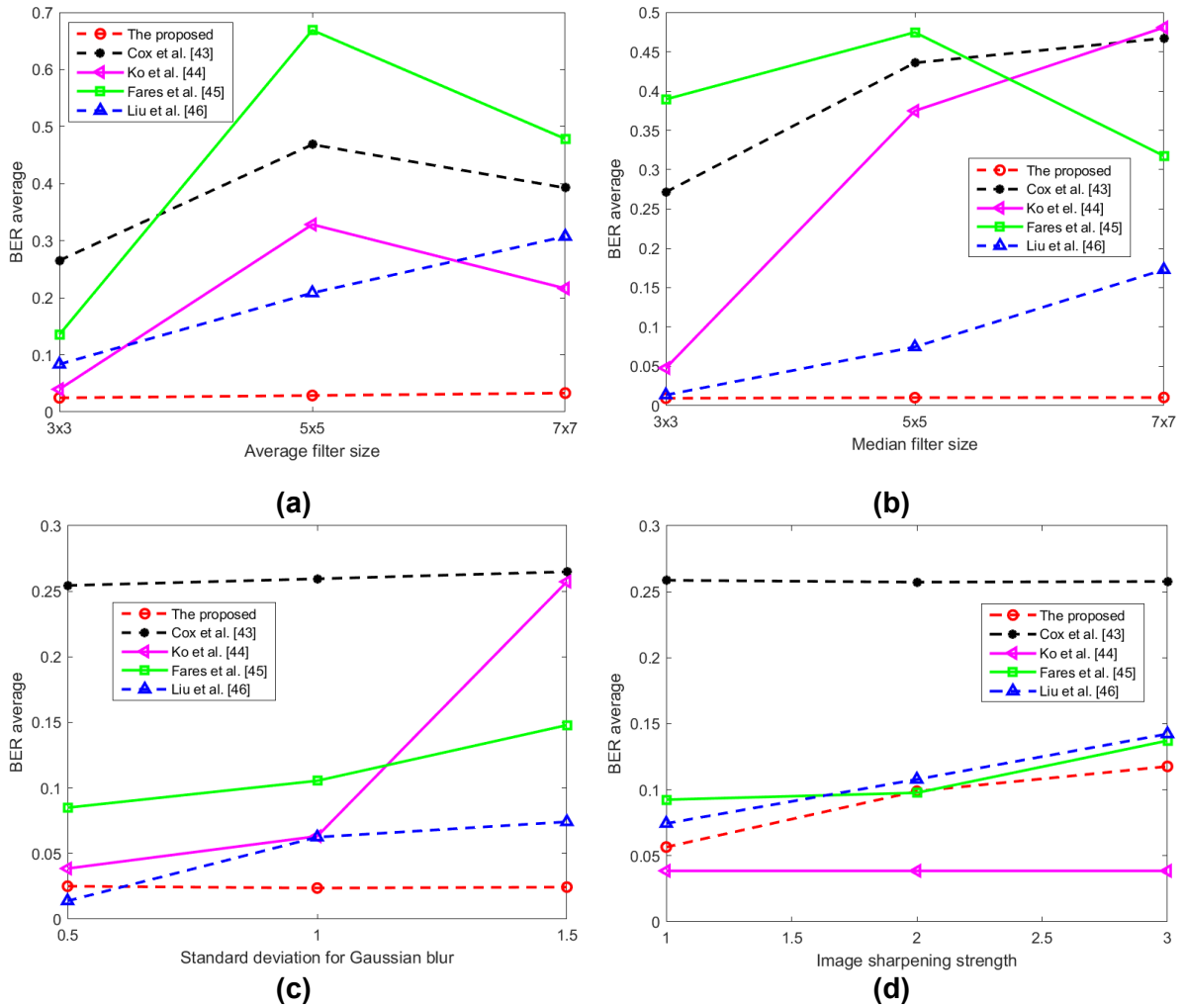

Fig. 19. Average BER values of the proposed watermarking method in comparison to related watermarking schemes under filter attacks.

4.3.4.3. Noises Attacks

Noise attacks represent a category of intentional manipulations aimed at degrading the quality and integrity of watermarked images. These attacks involve the addition of various forms of noise to the image, thereby destroying the extracted watermark. Two types of noise attacks, including salt and pepper noise and Gaussian noise, are added to the watermarked

image to assess the method's performance under noisy conditions. The watermarked image is subjected to salt and pepper as well as Gaussian noises, each with varying levels of noise intensity. In Fig. 22, the extracted watermark and its corresponding BER are presented for the five methods following exposure to salt and pepper noise with an intensity of 0.01, and Gaussian noise with an intensity of 0.001. Figure 23 illustrates the average BER values for the proposed watermarking algorithm and other watermarking algorithms across three distinct intensity levels. Notably, both the proposed method and Liu et al. [46] algorithm demonstrate the lowest BER values, indicating their superior performance.

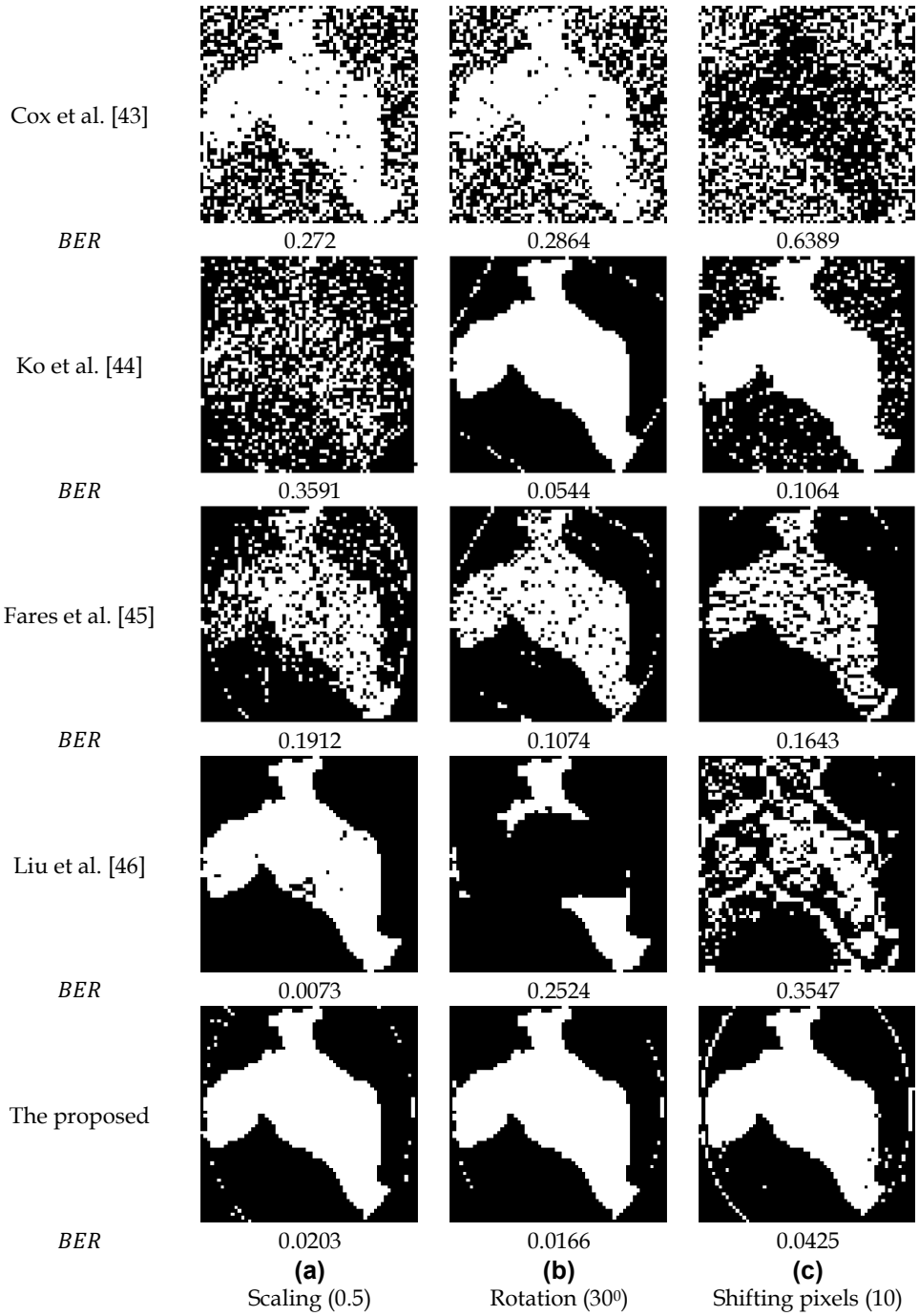

Fig. 20. Visual outcomes of the extracted watermarks using the proposed technique and the compared methods under geometric attacks.

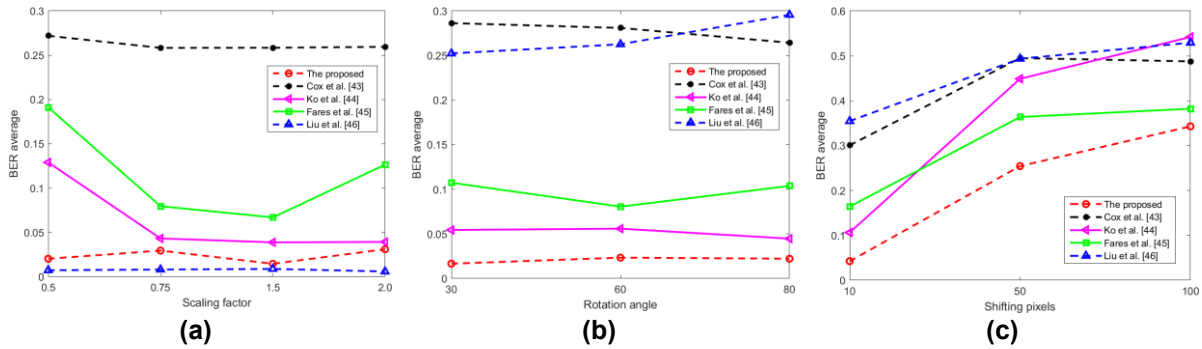

Fig. 21. Average BER values of the proposed method in comparison to related watermarking schemes under geometric attacks.

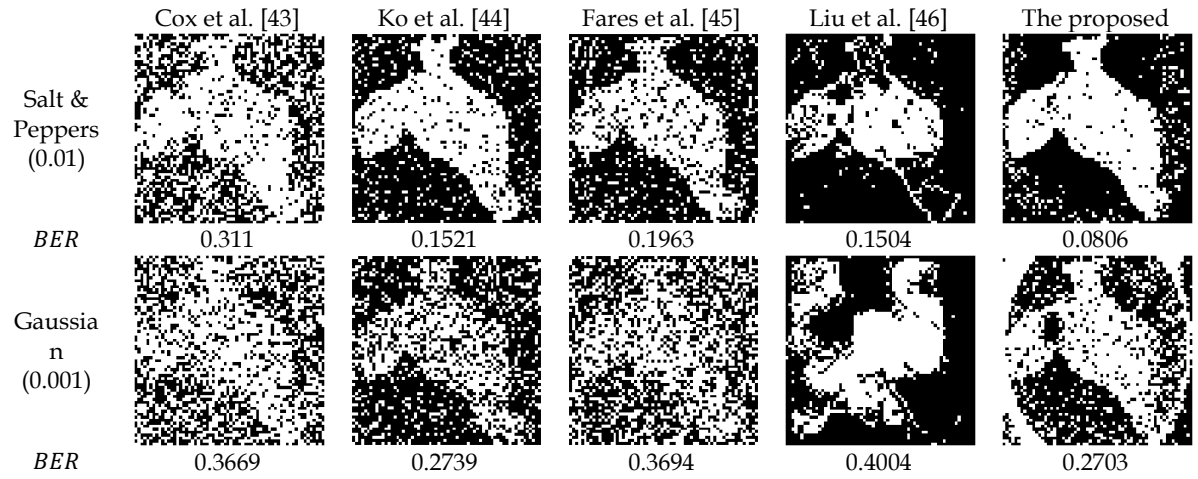

Fig. 22. Visual outcomes of the extracted watermarks using the proposed technique and the compared methods under noises attacks.

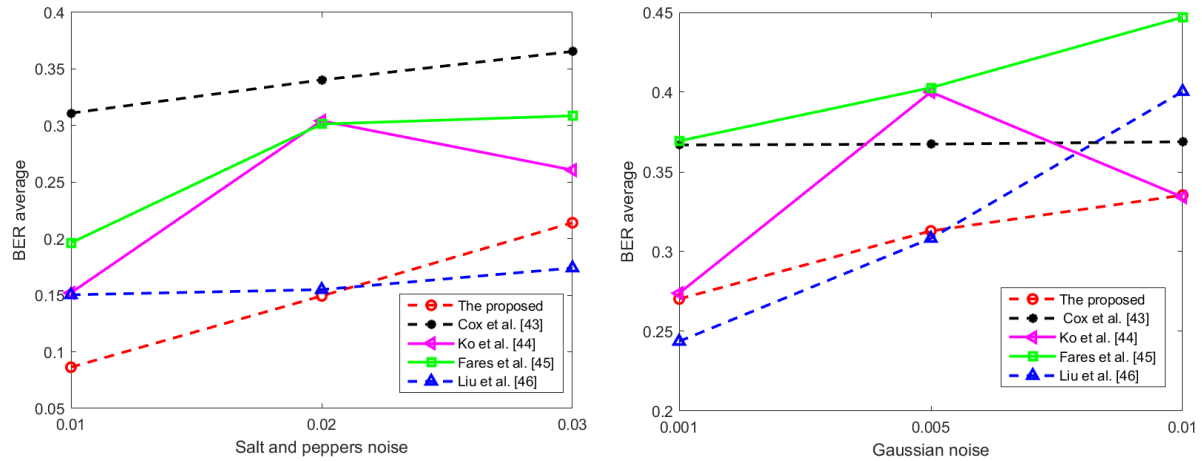

Fig. 23. Average BER values of the proposed method in comparison to related watermarking schemes under noises attacks.

4.3.4.4. Histogram equalization and Robustness {compression, cropping} attacks

Histogram equalization attack is an image enhancement process used to improve the visual quality and contrast of the watermarked image by redistributing pixel intensity values. When applied maliciously as part of an attack, histogram equalization can disrupt the embedded watermark, leading to a distortion of the hidden watermark. A JPEG (Joint Photographic Experts Group) compression attack is a technique used to reduce the file size of a watermarked image. This attack involves the intentional application of JPEG compression to watermarked images in order to assess the resilience of watermarking techniques against the

data loss and artifacts introduced by this specific compression algorithm. The cropping attack is a deliberate manipulation aimed at undermining the effectiveness of watermarking techniques by removing a portion of the watermarked image through cropping. This type of attack seeks to test the ability of watermarking methods to withstand the loss of image content while still enabling accurate watermark extraction. The extracted watermark is tested after applying histogram equalization, JPEG compression, and cropping attacks to the watermarked images. In Fig. 24, a visual example of the extracted watermark using the five methods is presented.

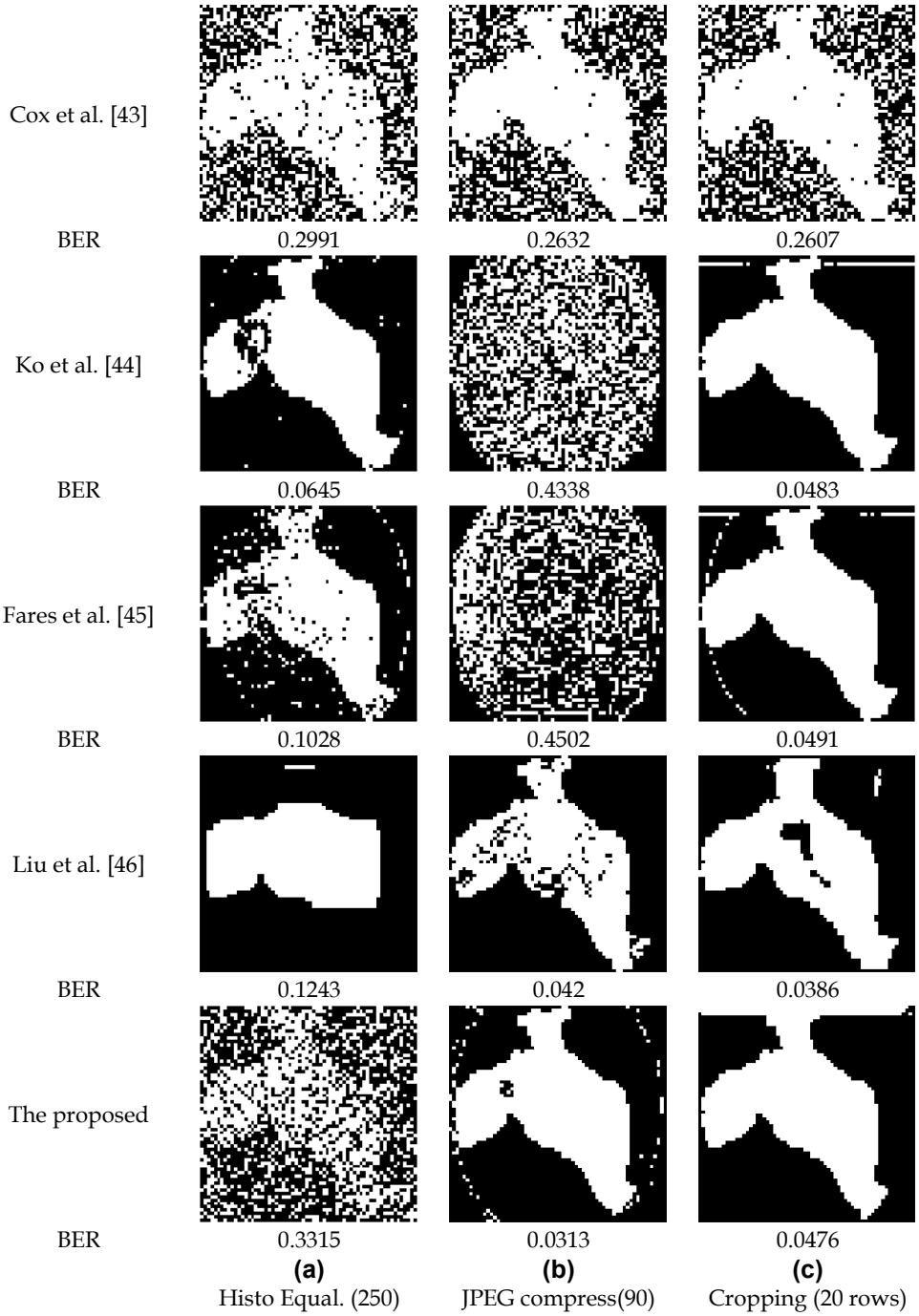

Fig. 24. Visual outcomes of the extracted watermarks using the proposed technique and the compared methods under histogram equalization and robustness attacks.

The watermarked image undergoes histogram equalization with 250 length bins in the second column, compression with a quality factor of 90 in the third column and cropping of 20 upper rows in the fourth column. The BER performance of the five methods is plotted in Fig. 25 for three different attack parameter values. Analysis of these two Figures reveals that the proposed method exhibits greater robustness against the JPEG compression attack, while it is not robust against the histogram equalization attack due to modifications in pixel values within each block.

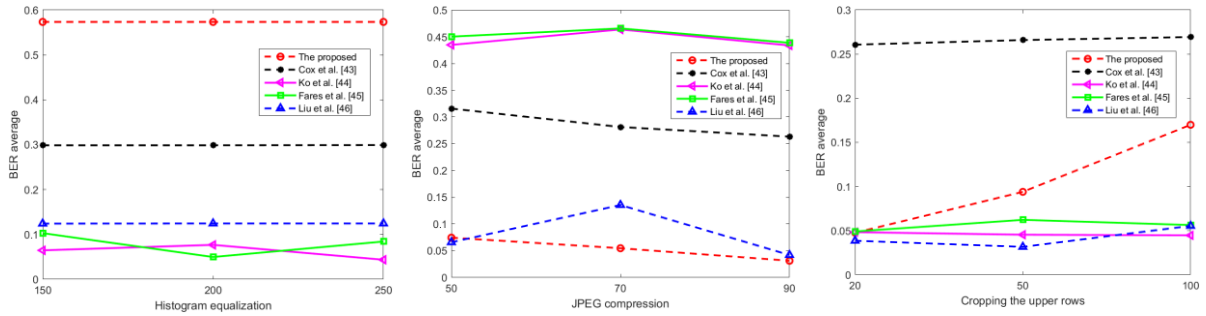

(a) (b) (c)

Fig. 25. Average BER values of the proposed method in comparison to related watermarking schemes under histogram equalization and robustness attacks.

Table 3 provides a summary of the comparison between the average correlation values of embedded and extracted chicken watermarks under various attacks, each with three different parameters, using the five methods. The table reveals that both the proposed watermarking algorithm and Ko et al. [44] exhibit correlation values that are remarkably close to unity across most attacks. This suggests that these two methods demonstrate greater robustness against a wide range of attack types. Notably, the proposed method showcases correlation values very close to one for average, median, blurring, shifting, salt & pepper, Gaussian, and JPEG compression attacks. This indicates that the proposed method outperforms other approaches in the majority of attacks.

5. CONCLUSION

In this article, we have introduced two algorithms designed for multi-channel color images. The first algorithm is a reconstruction method tailored for color images, and the second is a watermarking algorithm, also optimized for color images. Both algorithms operate in the transform domain based on discrete orthogonal Krawtchouk moments, which effectively capture intricate characteristics of color images. In the proposed reconstruction method, we derived weighted Krawtchouk polynomials from their traditional counterparts, enabling the use of a three-term recurrence relation based on these weighted polynomials for highly efficient color image reconstruction. For the watermarking scheme, we employed Krawtchouk moments and their inverses to insert and extract watermarks into and from host color images with remarkable accuracy. We rigorously tested both proposed algorithms on a medical image dataset containing 89 diabetic retinopathy images and four watermark images. We used commonly used metrics, including $MSE, PSNR, SSIM, BER,$ and $NCC,$ to assess the performance of our algorithms compared to eight state-of-the-art methods. Furthermore, we subjected our algorithms to testing for robustness against various image processing attacks, including 'salt & peppers' and Gaussian noises, as well as twelve watermarking attacks. The final results demonstrate that our proposed algorithms excel in delivering high-quality

reconstructed medical diabetic retinopathy images and exhibit robustness against image processing attacks.

Table 3. Correlation values average between embedded and extracted chicken watermarks under all attacks using the five methods.

Attack	Parameter	Cox et al. [43]	Ko et al. [44]	Fares et al. [45]	Liu et al. [46]	The proposed
Average	3×3	0.7643	**0.9917**	0.8606	0.8861	0.9681
	5×5	0.4974	0.6556	0.3107	0.7004	**0.9627**
	7×7	0.601	0.7772	0.4022	0.5565	**0.9575**
Median	3×3	0.7552	0.9806	0.4380	0.9822	**0.9876**
	5×5	0.543	0.6070	0.6440	0.9021	**0.9867**
	7×7	0.4893	0.5192	0.6352	0.7880	**0.9864**
Blurring	0.5	0.7729	**0.9933**	0.9308	0.9819	0.9679
	1.0	0.7682	0.9611	0.9020	0.9158	**0.9693**
	1.5	0.7640	0.7383	0.8432	0.8993	**0.9684**
Sharpening	1.0	0.7698	**0.9933**	0.9207	0.8987	0.9317
	2.0	0.7707	**0.9933**	0.9148	0.8498	0.8889
	3.0	0.7702	**0.9933**	0.8683	0.8002	0.8723
Scaling	0.5	0.7574	0.5186	0.7749	**0.9905**	0.9738
	0.75	0.7694	**0.9868**	0.9381	0.9895	0.9628
	1.5	0.7700	**0.9929**	0.9530	0.9886	0.981
Rotation	30^{o}	0.7459	0.9741	0.9017	0.5900	**0.9784**
	60^{o}	0.7500	**0.9725**	0.9390	0.5671	0.9694
	80^{0}	0.7641	**0.9865**	0.9049	0.4863	0.9713
Shifting	10	0.1910	0.8946	0.8216	0.4887	**0.9458**
	50	0.4509	0.6745	0.4176	0	**0.6854**
	100	0.4595	**0.6411**	0.6086	0	0.5356
Salt & Peppers	0.01	0.7115	0.8503	0.7875	0.7841	**0.894**
	0.02	0.6708	0.6753	0.6731	0.8020	**0.8177**
	0.03	0.6438	0.7082	0.6528	**0.7581**	0.742
Gaussian	0.001	0.6431	0.6682	0.6114	0.6588	**0.7101**
	0.005	0.6426	0.5685	0.5509	0.5946	**0.6972**
	0.010	0.6418	0.6263	0.5104	0.4846	**0.7047**
Histogram equalization	150	0.7300	**0.9586**	0.9077	0.8275	0.6346
	200	0.7296	0.9407	**0.9783**	0.8271	0.6346
	250	0.7302	**0.9868**	0.9318	0.8271	0.6346
JPEG Compression	50	0.7089	0.3718	0.4235	**0.9109**	0.9054
	70	0.7468	0.4575	0.4498	0.8069	**0.9318**
	90	0.7676	0.5055	0.4652	0.9442	**0.9596**
Cropping	20	0.7685	**0.9810**	0.9776	0.9492	0.9415
	50	0.7644	**0.9846**	0.9618	0.9591	0.8931
	100	0.7626	**0.9855**	0.9687	0.9285	0.8279

Acknowledgement: I would like to express my sincere gratitude to all those who supported me throughout the development of this work. I am especially grateful to the reviewers for their valuable time, insightful comments, and constructive suggestions, which greatly contributed to enhancing the quality of this paper.

REFERENCES

[1] N. Jing, Q. Liu, V. Sugumaran, ''A blockchain-based code copyright management system,'' *Information Processing & Management*, vol. 58, no. 3, 2021, doi: 10.1016/j.ipm.2021.102518.

[2] K. Fares, A. Khaldi, K. Redouane, E. Salah, ''DCT & DWT based watermarking scheme for medical information security,'' *Biomedical Signal Processing and Control*, vol. 66, p. 102403, 2021, doi: 10.1016/j.bspc.2020.102403.

[3] Q. Su, Y. Sun, X. Zhang, H. Wang, G. Wang, T. Yao, ''A watermarking scheme for dual-color images based on URV decomposition and image correction,'' *International Journal of Intelligent Systems*, vol. 37, no. 10, 2022, pp. 7548–7570, doi: 10.1002/int.22893.

[4] L. Rakhmawati, W. Wirawan, S. Suwadi, C. Delpha, P. Duhamel, ''Blind robust image watermarking based on adaptive embedding strength and distribution of quantified coefficients,'' *Expert Systems with Applications*, vol. 187, p. 115906, 2022, doi: 10.1016/j.eswa.2021.115906.

[5] H. Hu, L. Hsu, H. Chou, ''An improved SVD-based blind color image watermarking algorithm with mixed modulation incorporated,'' *Information Sciences*, vol. 519, 2022, pp. 161–182, doi: 10.1016/j.ins.2020.01.019.

[6] J. Wang, D. Wu, L. Li, J. Zhao, H. Wu, Y. Tang, ''Robust periodic blind watermarking based on sub-block mapping and block encryption,'' *Expert Systems with Applications*, vol. 224, p. 119981, 2023, doi: 10.1016/j.eswa.2023.119981.

[7] G. Liu, H. Wang, C. Miao, ''A three-dimensional text image watermarking model based on multilayer overlapping of extracted two-dimensional information,'' *Information Processing & Management*, vol. 60, no. 1, p. 103122, 2023, doi: 10.1016/j.ipm.2022.103122.

[8] A. Daoui, M. Yamni, H. Karmouni, M. Sayyouri, H. Qjidaa, ''Biomedical signals reconstruction and zero-watermarking using separable fractional order Charlier–Krawtchouk transformation and Sine Cosine Algorithm,'' *Signal Processing*, vol. 180, p. 107854, 2021, doi: 10.1016/j.sigpro.2020.107854.

[9] J. Lang, Z. Zhang, ''Blind digital watermarking method in the fractional Fourier transform domain,'' *Optics and Lasers in Engineering*, vol. 53, 2014, pp. 112-121, doi: 10.1016/j.optlaseng.2013.08.021.

[10] Z. Xia, X. Wang, X. Li, C. Wang, S. Unar, M. Wang, T. Zhao, ''Efficient copyright protection for three CT images based on quaternion polar harmonic Fourier moments,'' *Signal Processing*, vol. 164, pp. 368–379, 2019, doi: 10.1016/j.sigpro.2019.06.025.

[11] X. Liu, Y. Wang, Z. Sun, L. Wang, R. Zhao, Y. Zhu, B. Zou, Y. Zhao, H. Fang, ''Robust and discriminative zero-watermark scheme based on invariant features and similarity-based retrieval to protect large-scale DIBR 3D videos,'' *Information Sciences,* vol. 542, pp. 263–285, 2021, doi: 10.1016/j.ins.2020.06.066.

[12] D. Wu, M. Wang, J. Zhao, J. Wang, M. Zhong, H. Zheng, S. Hu, Y. Tang, C. Qu, ''Color zero-watermarking algorithm for medical images based on BEMD-Schur decomposition and color visual cryptography,'' *Security and Communication Networks*, p. 7081194, 2021, doi: 10.1155/2021/7081194.

[13] B. Yang, G. Li, H. Zhang, M. Dai, ''Rotation and translation invariants of Gaussian–Hermite moments,'' Pattern Recognition Letters, vol. 32, no. 39, pp. 1283–1298, 2011, doi: 10.1016/j.patrec.2011.03.012.

[14] H. Karmouni, T. Jahid, A. Hmimid, M. Sayyouri, H. Qjidaa, ''Fast computation of inverse Meixner moments transform using Clenshaw's formula,'' *Multimedia Tools and Applications*, vol. 78, pp. 31245–31265, 2019, doi: 10.1007/s11042-019-07961-y.

[15] H. Amakdouf, A. Zouhri, M. EL Mallahi, H. Qjidaa, ''Color image analysis of quaternion discrete radial Krawtchouk moments,'' *Multimedia Tools and Applications,* vol. 79, pp. 26571–26586, 2020, doi: 10.1007/s11042-020-09120-0.

[16] A. Daoui, H. Karmouni, M. Sayyouri, H. Qjidaa, ''Fast and stable computation of higher-order Hahn polynomials and Hahn moment invariants for signal and image analysis,'' *Multimedia Tools and Applications,* vol. 80, pp. 32947–32973, 2021, doi: 10.1007/s11042-021-11206-2.

[17] A. Singh, B. Kumar, G. Singh, A. Mohan, *Medical image watermarking: Techniques and Applications*, Springer International Publishing AG, 2017.

[18] S. Mousavi, A. Naghsh , S. Abu-Bakar, ''Watermarking techniques used in medical images: a survey,'' *Journal of Digit Imaging*, vol. 27, no. 6, pp. 714-29, 2014,doi: 10.1007/s10278-014-9700-5.

[19] H. Nyeem, W. Boles, C. Boyd, ''A review of medical image watermarking requirements for teleradiology,'' *Journal of Digit Imaging,* vol. 26, pp. 326–343, 2013, doi: 10.1007/s10278-012-9527-x

[20] J. Abraham, V. Paul, ''An imperceptible spatial domain color image watermarking scheme,'' *Journal of King Saud University - Computer and Information Sciences*, vol. 31, no. 1, pp. 125-133, 2019, doi: 10.1016/j.jksuci.2016.12.004.

[21] J. Fridrich, M. Goljan, R. Du, ''Lossless data embedding for all image formats,'' Security and Watermarking of Multimedia Contents IV, 2002, doi: 10.1117/12.465317.

[22] M. Eltoukhy, A. Khedr, M. Abdel-Aziz, K. Hosny, ''Robust watermarking method for securing color medical images using Slant-SVD-QFT transforms and OTP encryption,'' *Alexandria Engineering Journal*, vol. 78, pp. 517-529, 2013, doi:10.1016/j.aej.2023.07.068.

[23] D. Wu, L. Li, J. Wang, P. Ma, Z. Wang, H. Wu, ''Robust zero-watermarking scheme using DT CWT and improved differential entropy for color medical images,'' Jou*rnal of King Saud University - Computer and Information Sciences*, vol. 35, no. 8, p. 101708, 2023, doi: 10.1016/j.jksuci.2023.101708.

[24] R. Eswaraiah, E. Reddy, ''Robust medical image watermarking technique for accurate detection of tampers inside region of interest and recovering original region of interest,'' *IET Image Processing*, vol. 9, no. 8, pp. 515-625, 2015, doi: 10.1049/iet-ipr.2014.0986.

[25] A. Bera, P. Klesk, D. Sychel, ''Constant-time calculation of Zernike moments for detection with rotational invariance,'' *IEEE Transactions on Pattern Analysis and Machine Intelligence*, vol. 41, no. 3, pp. 537–551, 2018, doi: 10.1109/TPAMI.2018.2803828.

[26] H. Zhang, H. Shu, G. Coatrieux, J. Zhu, Q. J. Wu, Y. Zhang, H. Zhu, L. Luo, ''Affine Legendre moment invariants for image watermarking robust to geometric distortions,'' IEEE Transactions on Image Processing, vol. 20, no. 8, pp. 2189–2199, 2011, doi:10.1109/tip.2011.2118216.

[27] X. Wang, P. Niu, H. Yang, C. Wang, A. Wang, ''A new robust color image watermarking using local quaternion exponent moments,'' *Information Sciences*, vol. 277, 731–754, 2014, doi: 10.1016/j.ins.2014.02.158.

[28] G. Gao, G. Jiang, ''Bessel-Fourier moment-based robust image zero-watermarking,'' *Multimedia Tools Applications,* vol. 74, pp. 841–858, 2015, doi: 10.1007/s11042-013-1701-8.

[29] C. Wang, X. Wang, Z. Xia, C. Zhang, ''Ternary radial harmonic Fourier moments based robust stereo image zero-watermarking algorithm,'' *Information Sciences*, vol. 470, pp. 109–120, 2014, doi: 10.1016/j.ins.2018.08.028.

[30] W. Wang, Y. Li, S. Liu, ''A polar complex exponential transform-based zero-watermarking for multiple medical images with high discrimination,'' *Security and Communication Networks*, 2021, p. 6615678, 2021, doi: 10.1155/2021/6615678.

[31] X. Kang, F. Zhao, Y. Chen, G. Lin, C. Jing, ''Combining polar harmonic transforms and 2D compound chaotic map for distinguishable and robust color image zero-watermarking algorithm,'' *Journal of Visual Communication and Image Representation*, vol. 70, p. 102804, 2020, doi: 10.1016/j.jvcir.2020.102804.

[32] Z. Xia, X. Wang, B. Han, Q. Li, X. Wang, C. Wang, T. Zhao, ''Color image triple zero-watermarking using decimal-order polar harmonic transforms and chaotic system,'' *Signal Processing*, vol. 180, p. 107864, 2021, doi: 10.1016/j.sigpro.2020.107864.

[33] H. Yang, S. Qi, P. Niu, X. Wang, ''Color image zero-watermarking based on fast quaternion generic polar complex exponential transform,'' *Signal Processing,* vol. 82, p. 115747, 2020, doi: 10.1016/j.image.2019.115747.

[34] M. Yamni, H. Karmouni, M. Sayyouri, H. Qjidaa, ''Robust zero-watermarking scheme based on novel quaternion radial fractional Charlier moments,'' *Multimedia Tools and Applications,* vol. 80, pp. 21679–21708, 2021, doi: 10.1007/s11042-021-10717-2.

[35] F. Kahlessenane, A. Khaldi, R. Kafi, S. Euschi, ''A DWT based watermarking approach for medical image protection, *Journal of Ambient Intelligence and Humanized Computing*, vol. 12, pp. 2931–2938, 2021, doi: 10.1007/s12652-020-02450-9.

[36] C. Dong, Y. Chen, J. Li Y. Bai, ''Zero watermarking for medical images based on DFT and LFSR,'' IEEE International Conference on Computer Science and Automation Engineering, 2012, doi: 10.1109/CSAE.2012.6272540.

[37] N. Zermi, A. Khaldi, M. Kafi, F. Kahlessenane, S. Euschi, ''Robust SVD-based schemes for medical image watermarking,'' *Microprocessors and Microsystems*, vol. 84, p. 104134, 2021, doi: 10.1016/j.micpro.2021.104134.

[38] T. Kauppi, V. Kalesnykiene, J. Kamarainen, L. Lensu, I. Sorri, A. Raninen, R. Voutilainen, H. Uusitalo, H. Kälviäinen, J. Pietilä, ''DIARETB1 diabetic retinopathy database and evaluation protocol,'' British Machine Vision Conference, 2007, doi: api.semanticscholar.org/CorpusID:15483141.

[39] H. Ren, Z. Ping, W. Bo, W. Wu, Y. Sheng, ''Multi-distortion-invariant image recognition with radial harmonic Fourier moments,'' *Journal of the Optical Society of America A*, vol. 20, no. 4, pp. 631-637, 2023, doi: 10.1364/JOSAA.20.000631.

[40] H. Hu, Y. Zhang, C. Shao, Q. Ju, ''Orthogonal moments based on exponent functions: Exponent-Fourier moments,'' *Pattern Recognition*, vol. 47, no. 8, pp. 2596-2606, 2014, doi: 10.1016/j.patcog.2014.02.014.

[41] H. Karmouni, A. Hmimid, T. Jahid, M. Sayyouri, H. Qjidaa, A. Rezzouk, ''Fast and stable computation of the Charlier moments and their inverses using digital filters and image block representation,'' *Circuits, Systems, and Signal Processing*, vol. 37, pp. 4015–4033, 2018, doi: 10.1007/s00034-018-0755-2.

[42] R. Mukundan, S. Ong, P. Lee, ''Image analysis by Tchebichef moments,'' *IEEE Transactions on Image processing*, vol. 10, no. 9, pp. 1357 – 1364, 2001, doi: 10.1109/83.941859.

[43] I. Cox, J. Kilian, F. Lighton, T. Shamoon, ''Secure spread spectrum watermarking for multimedia,'' *IEEE Transactions on Image Processing*, vol. 6, no. 12, pp. 1673 – 1687, 1997, doi: 10.1109/83.650120.

[44] H. Ko, C. Huang, G. Horng, S. Wang, ''Robust and blind image watermarking in DCT domain using inter-block coefficient correlation,'' *Information Sciences*, vol. 517, pp. 128-147, 2020, doi: 10.1016/j.ins.2019.11.005.

[45] K. Fares, K. Amine, E. Salah, ''A robust blind color image watermarking based on Fourier transform domain,'' *Optik*, vol. 208, p. 164562, 2020, doi: 10.1016/j.ijleo.2020.164562.

[46] J. Liu, J. Huang, Y. Lou, L. Cao, S. Yang, D. Wei, R. Zhou, ''An optimized image watermarking method based on HD and SVD in DWT domain,'' *IEEE Access,* vol. 7, pp. 80849-80860, 2019, doi: 10.1109/ACCESS.2019.2915596

[47] I. Prathap, V. Natarajan, R. Anitha, ''Hybrid robust watermarking for color images,'' *Computers & Electrical Engineering*, vol. 40, no. 3, pp. 920–930, 2014, doi: 10.1016/j.compeleceng.2014.01.006.

[48] A. Shabir, J. Sheikh, N. Loan, G. Bhat, ''Robust and blind watermarking technique in DCT domain using inter-block coefficient differencing,'' *Digital Signal Processing*, vol. 53, p. 11-24, 2016, doi: 10.1016/j.dsp.2016.02.005.

[49] S. Lin, S. Shie, J. Guo, ''Improving the robustness of DCT-based image watermarking against JPEG compression,'' *Computer Standards & Interfaces*, vol. 32, pp. 54–60, 2010, doi: 10.1016/j.csi.2009.06.004.

[50] A. Kamrani, K. Zenkouar, S. Najah, ''A new set of image encryption algorithms based on discrete orthogonal moments and Chaos theory,'' *Multimedia Tools and Applications,* vol. 79, pp. 20263–20279, 2020, doi: 10.1007/s11042-020-08879-6.

[51] M. Yamni, A. Daoui, O. El ogri, H. Karmouni, M. Sayyouri, H. Qjidaa, J. Flusser, ''Fractional Charlier moments for image reconstruction and image watermarking,'' *Signal Processing*, vol. 171, p. 107509, 2020, doi: 10.1016/j.sigpro.2020.107509.